Supplementary Information

Supported Core@Shell Electrocatalysts for Fuel Cells: Close Encounter with Reality

Seung Jun Hwang, Sung Jong Yoo, Jungho Shin, Yong-Hun Cho, Jong Hyun Jang, Eunae Cho, Yung-Eun Sung, Suk Woo Nam, Tae-Hoon Lim, Seung-Cheol Lee*, and, Soo-Kil Kim*

*To whom correspondence should be addressed. E-mail: leesc@kist.re.kr; sookilkim@cau.ac.kr

1. Synthesis

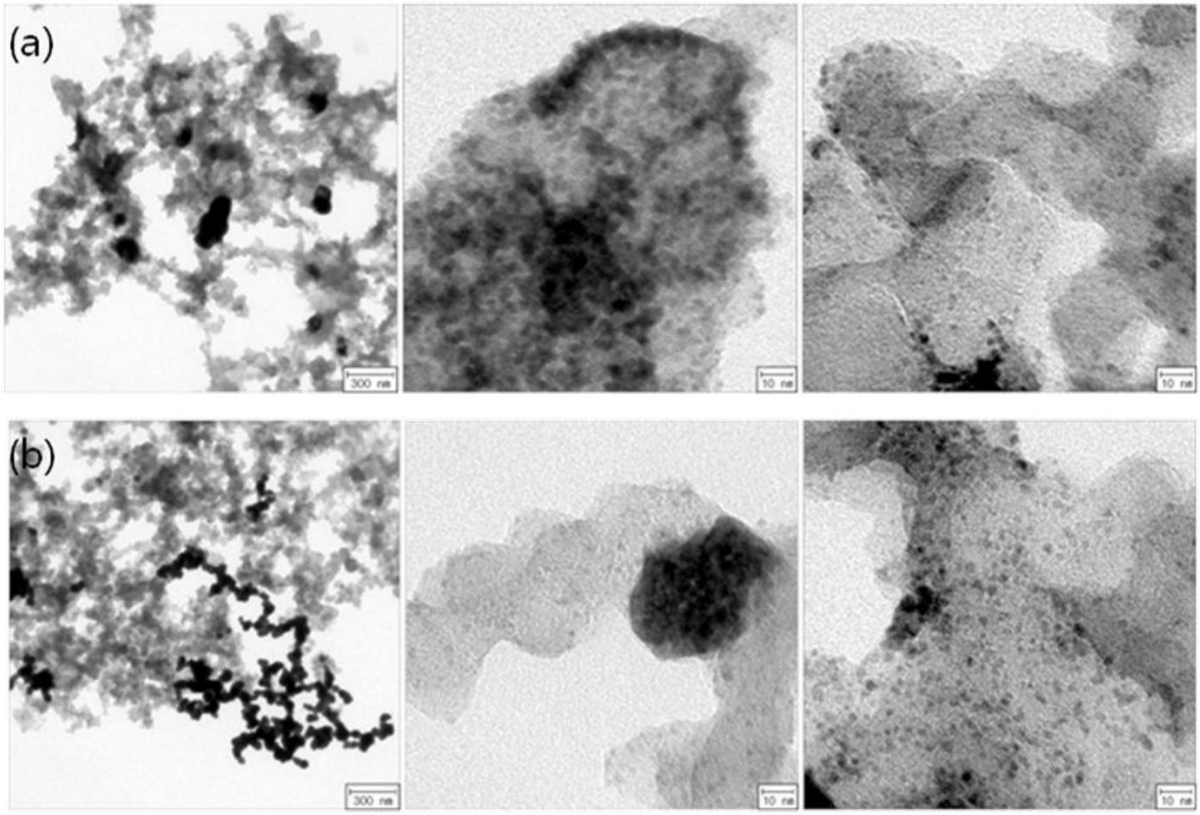

Fig. S1. TEM images of Pd/C nanoparticles. (a) $Pd(acac)_2$, Oleylamine, $NaBH_4$, and 1,2-propandiol was used as precursor, stabilizer, reducing agent, and solvent, (b)$Pd(acac)_2$, Oleylamine, t-butylamine borane, 1,2-propandiol was used at 95 ^{o}C as precursor, stabilizer, reducing agent, and solvent.

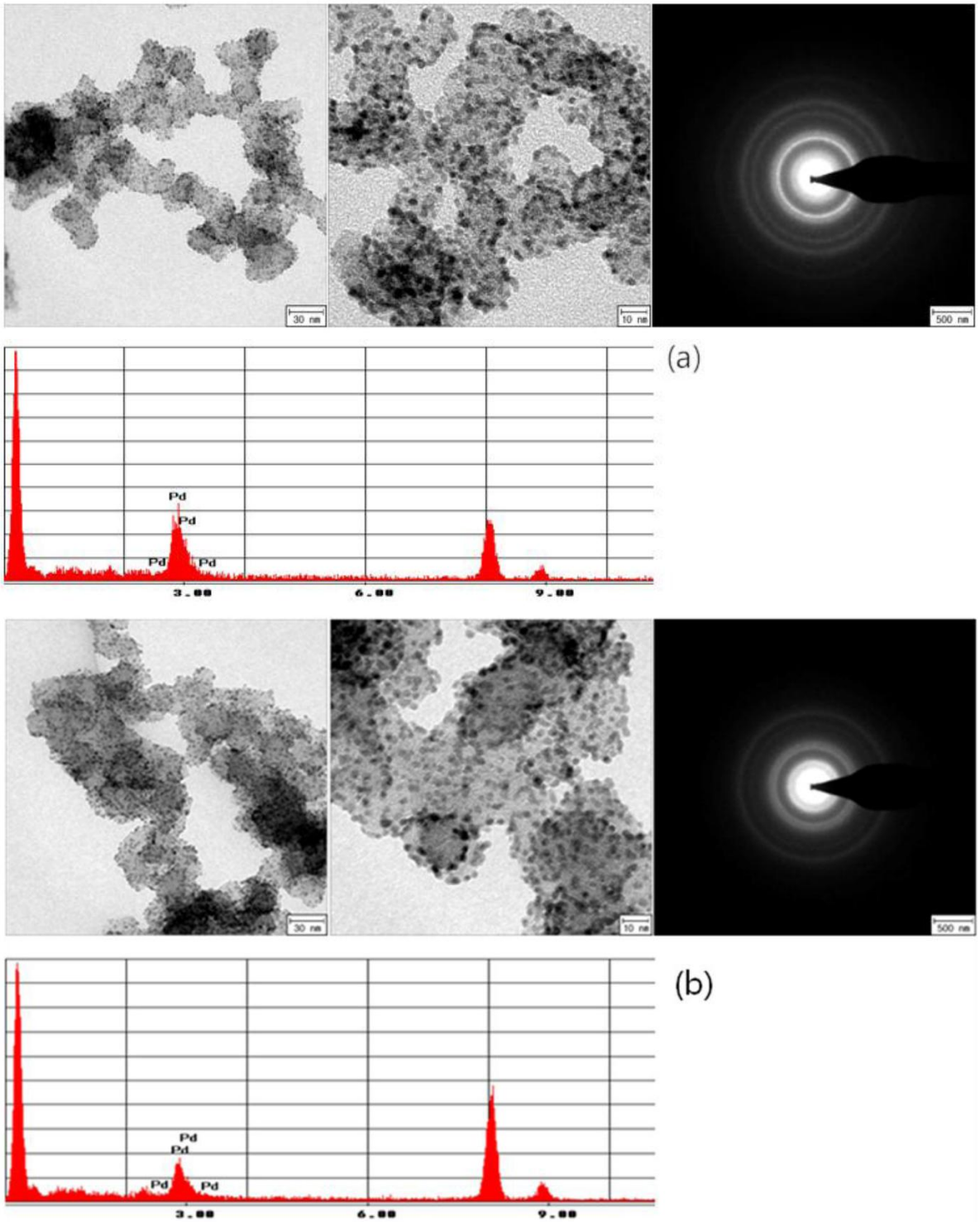

Fig. S2. TEM images of Pd/C nanoparticles. (a) $Pd(acac)_2$, Oleylamine, t-butylamine borane, benzyl ether was used at room temperature, (b) $Pd(acac)_2$, Oleylamine, t-butylmine borane, benzyl ether was used at 95 ^{o}C.

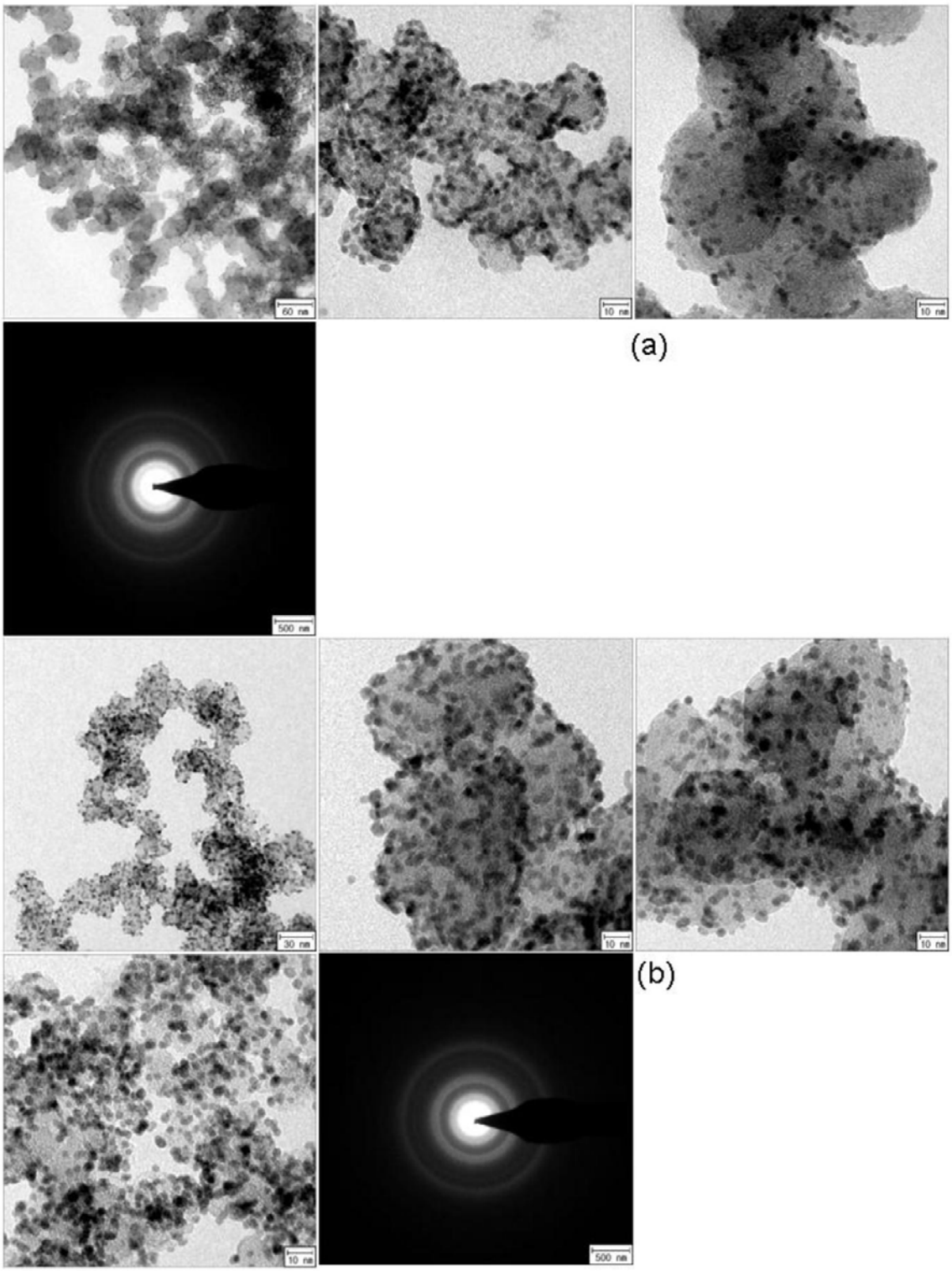

Fig. S3. TEM images of Pd/C nanoparticles without using stabilizer. (a) $Pd(acac)_2$,t-butylamine borane, benzyl ether was used at room temperature, (b) $Pd(acac)_2$,t-butylmine borane, benzyl ether was used at 95 ^oC.

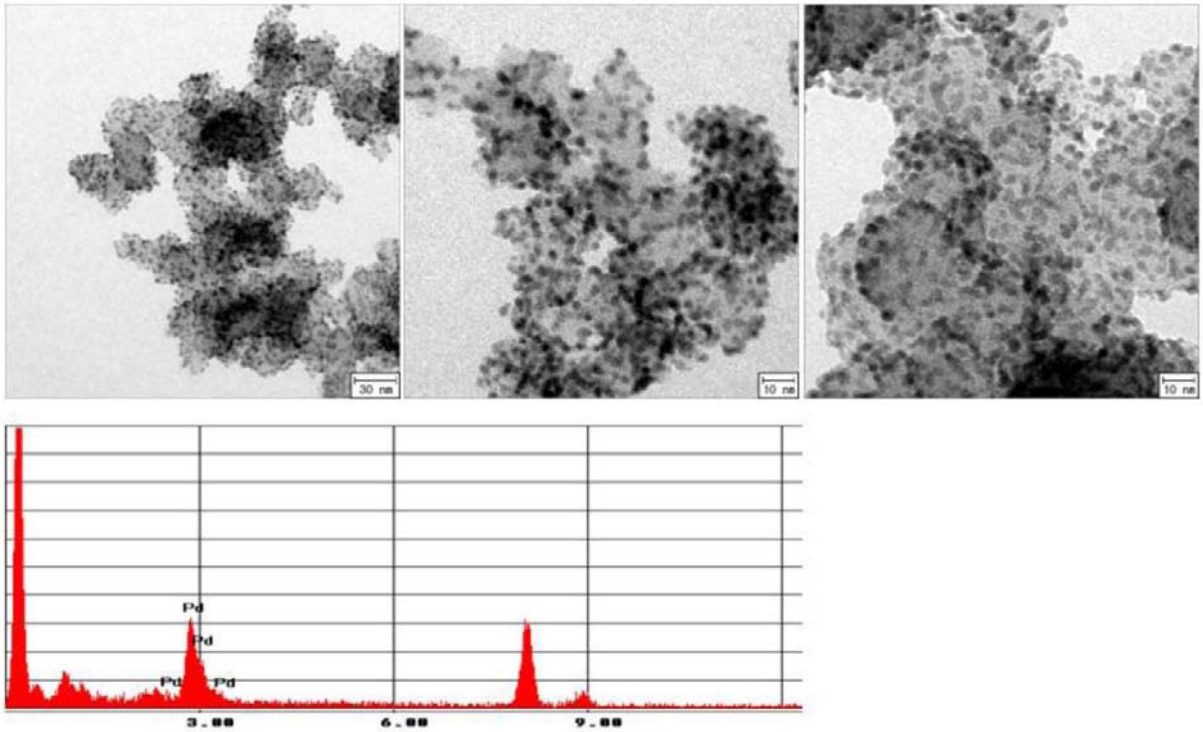

Fig. S4. TEM images of Pd_3Cu_1/C nanoparticles without using stabilizer. $Pd(acac)_2$, $Cu(acac)_2$, t-butylamine borane, benzyl ether was used at 95 ^oC.

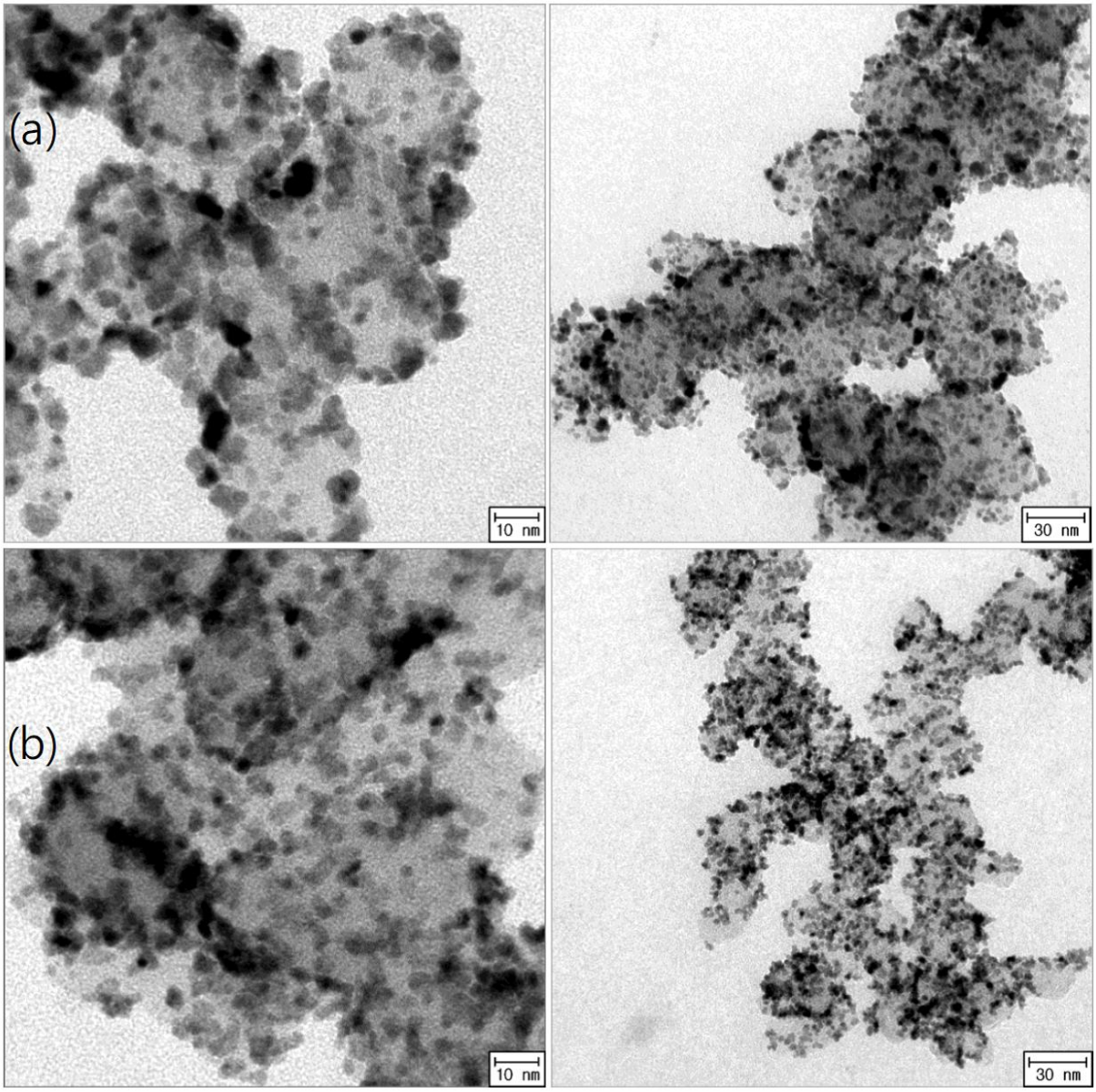

Fig. S5. TEM images of Pd_3Cu_1@Pt/C nanoparticles with using different reducing agent. (a) Ascorbic acid (b) Hantzsch ester.

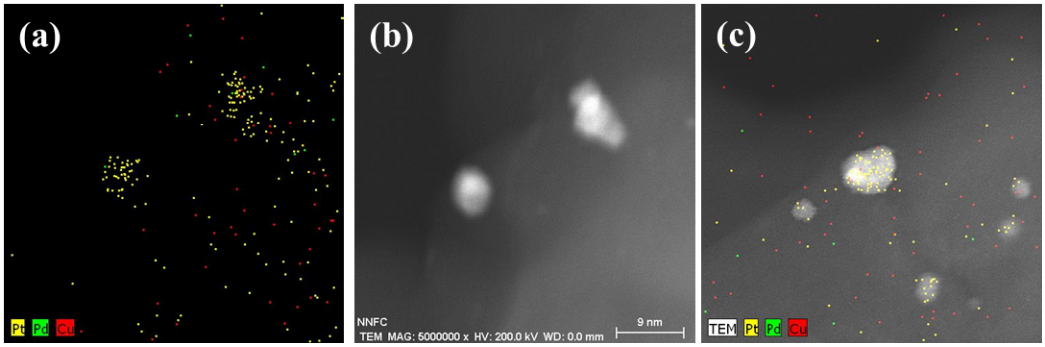

Fig. S6. Pt, Pd, and Cu maps extracted from the electron energy loss spectroscopic images of the particle in Pd_3Cu_1@Pt/C synthesized by (a), (b) ascorbic acid and (c) sodium borohydride.

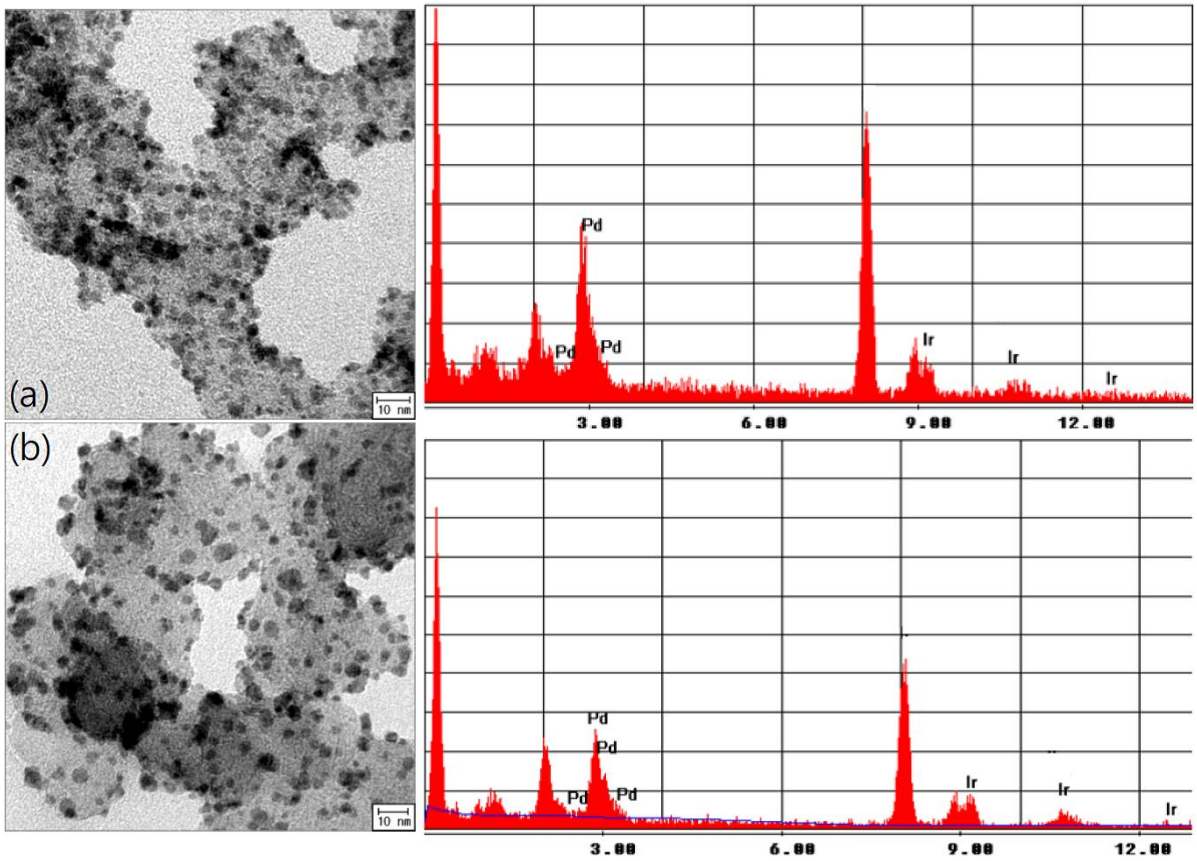

Fig. S7. TEM images of (a) Pd@Ir/C and (b) Pd@PdIr/C nanoparticles.

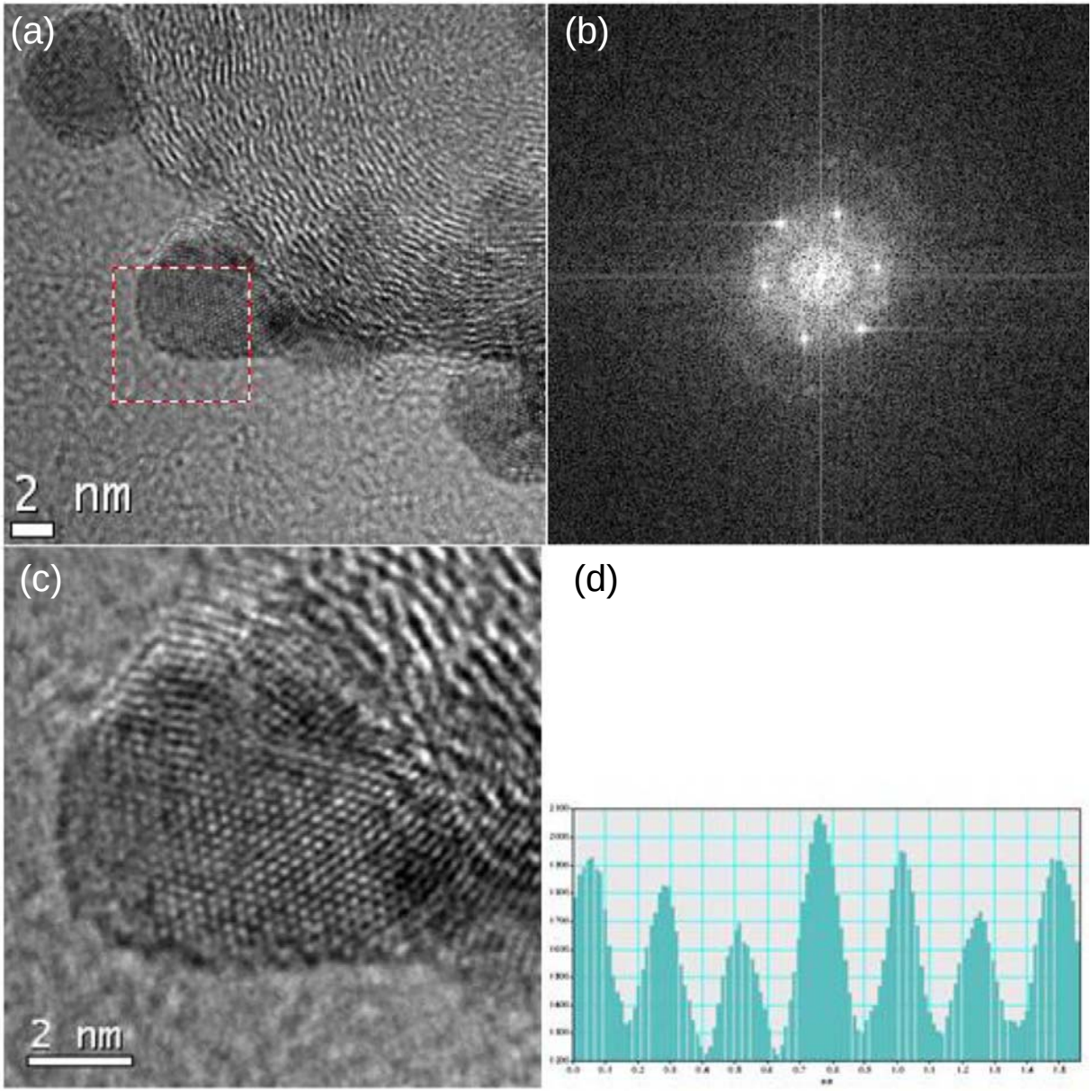

Fig. S8. (a) High Resolution TEM image of fabricated Pd/C nanoparticles using $Pd(acac)_2$, t-butylamine borane, benzyl ether at 95°C in the absence of stabilizer, (b) its FFT (fast Fourier Transform), (c) its magnified image and (d) intensity line profiles.

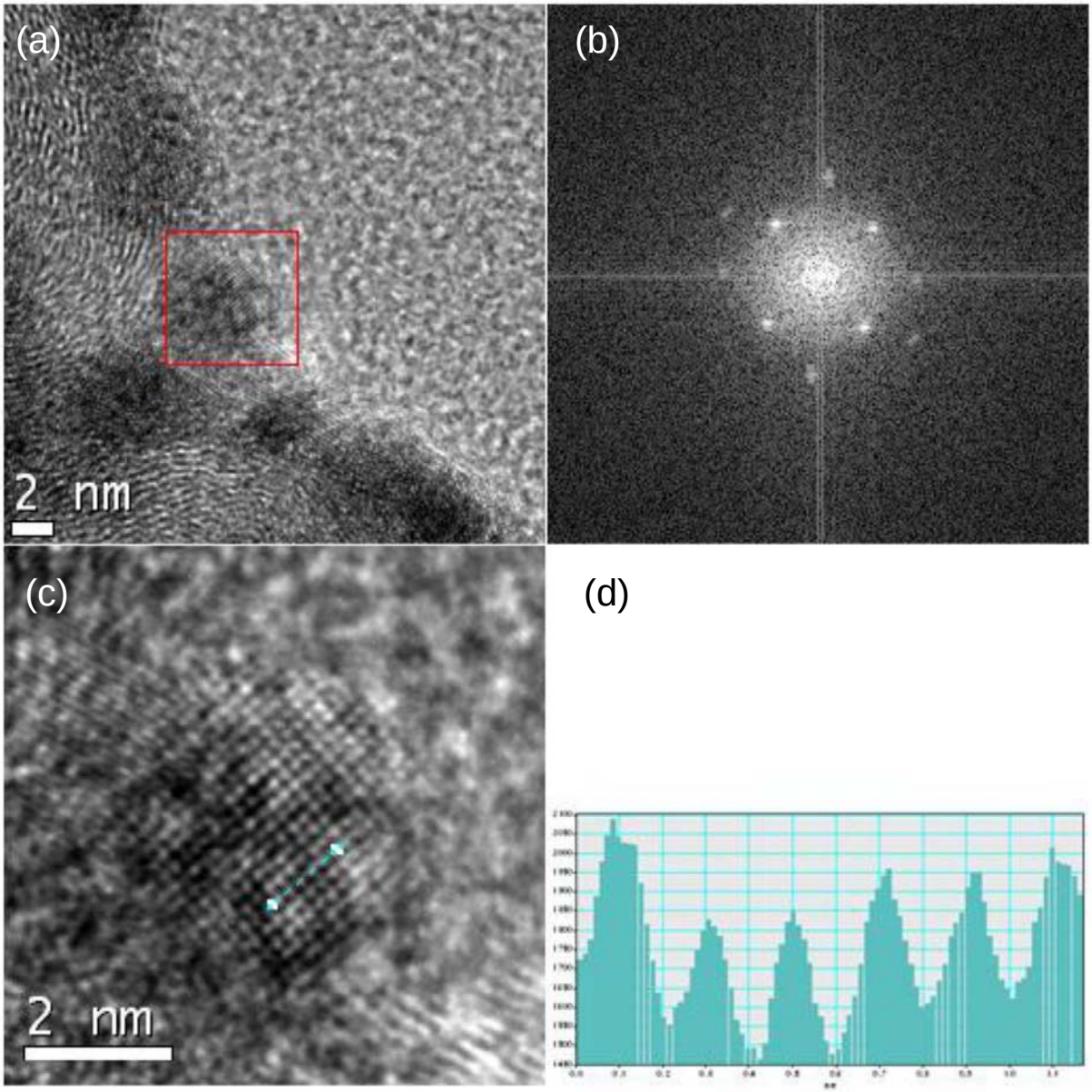

Fig. S9. (a) High Resolution TEM images of fabricated PdCu/C nanoparticles using $Pd(acac)_2$, $Cu(acac)_2$, t-butylamine borane, benzyl ether at 95°C in the absence of stabilizer, (b) its FFT (fast Fourier Transform), (c) its magnified image and (d) intensity line profiles.

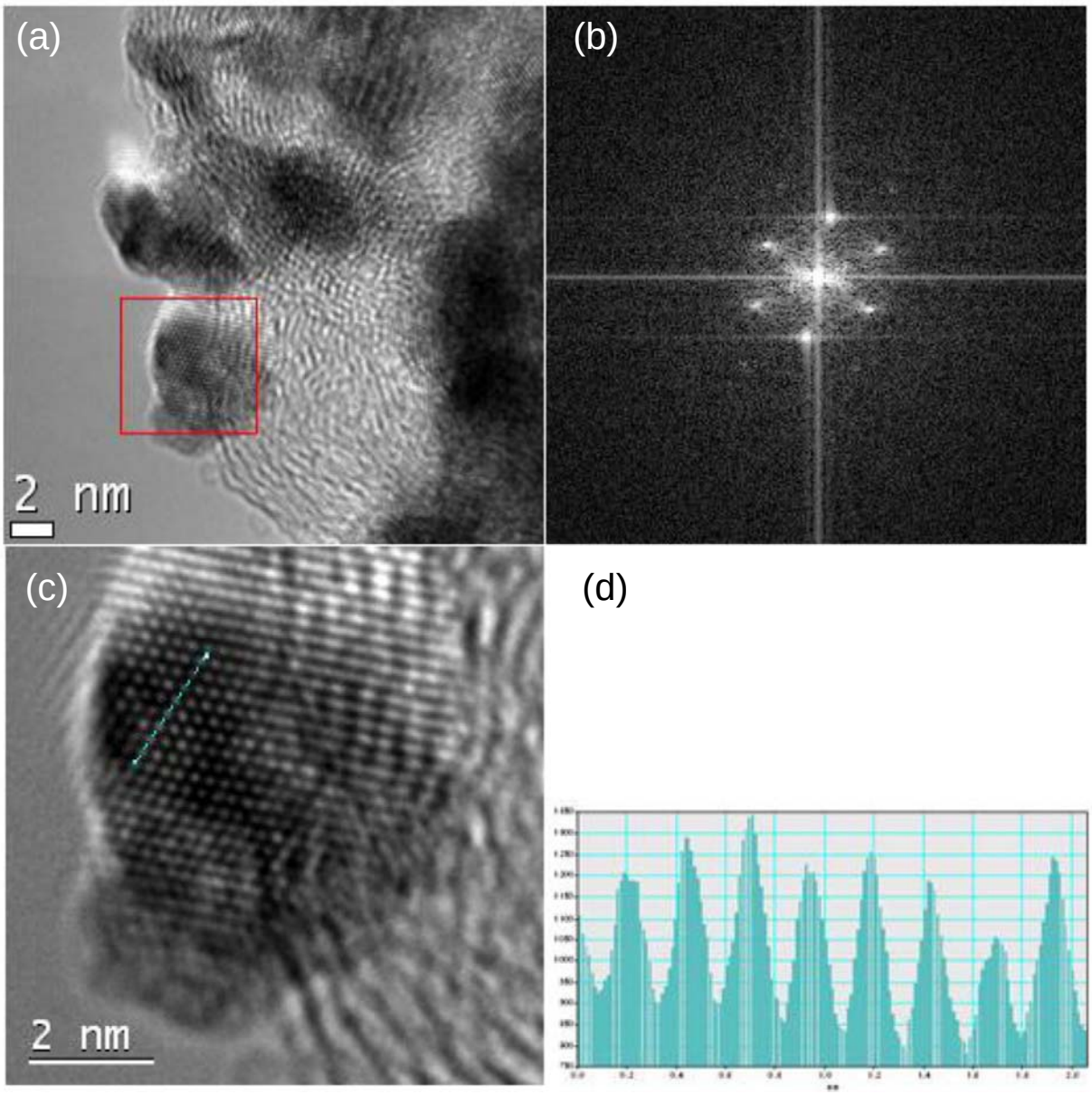

Fig. S10. (a) High Resolution TEM image of fabricated Pd_3Cu_1@Pt/C nanoparticles using Pd_3Cu_1/C, $H_2PtCl_6{\cdot}6H_2O$, Hantzsch ester, ethanol at 80^oC, (b) its FFT (fast Fourier Transform), (c) its magnified image and (d) intensity line profiles.

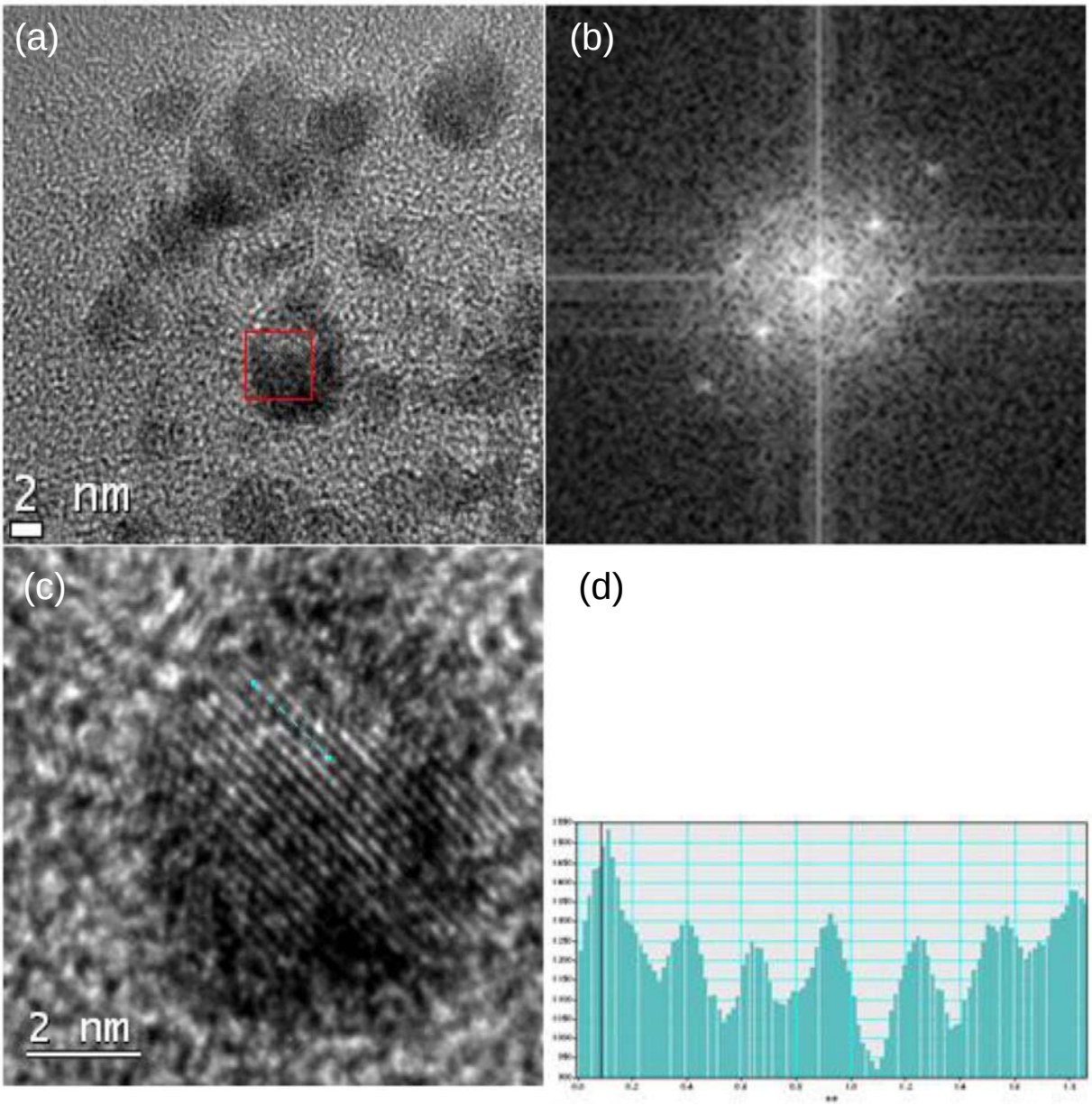

Fig. S11. (a) High Resolution TEM image of fabricated Pd@PdIr/C nanoparticles using Pd/C, K_2PdCl_4, $IrCl_3 \cdot H_2O$, Hantzsch ester, ethanol at 80^oC, (b) its FFT (fast Fourier Transform), (c) its magnified image and (d) intensity line profiles.

2. **Physical Characterization**

2.1. X-ray diffraction

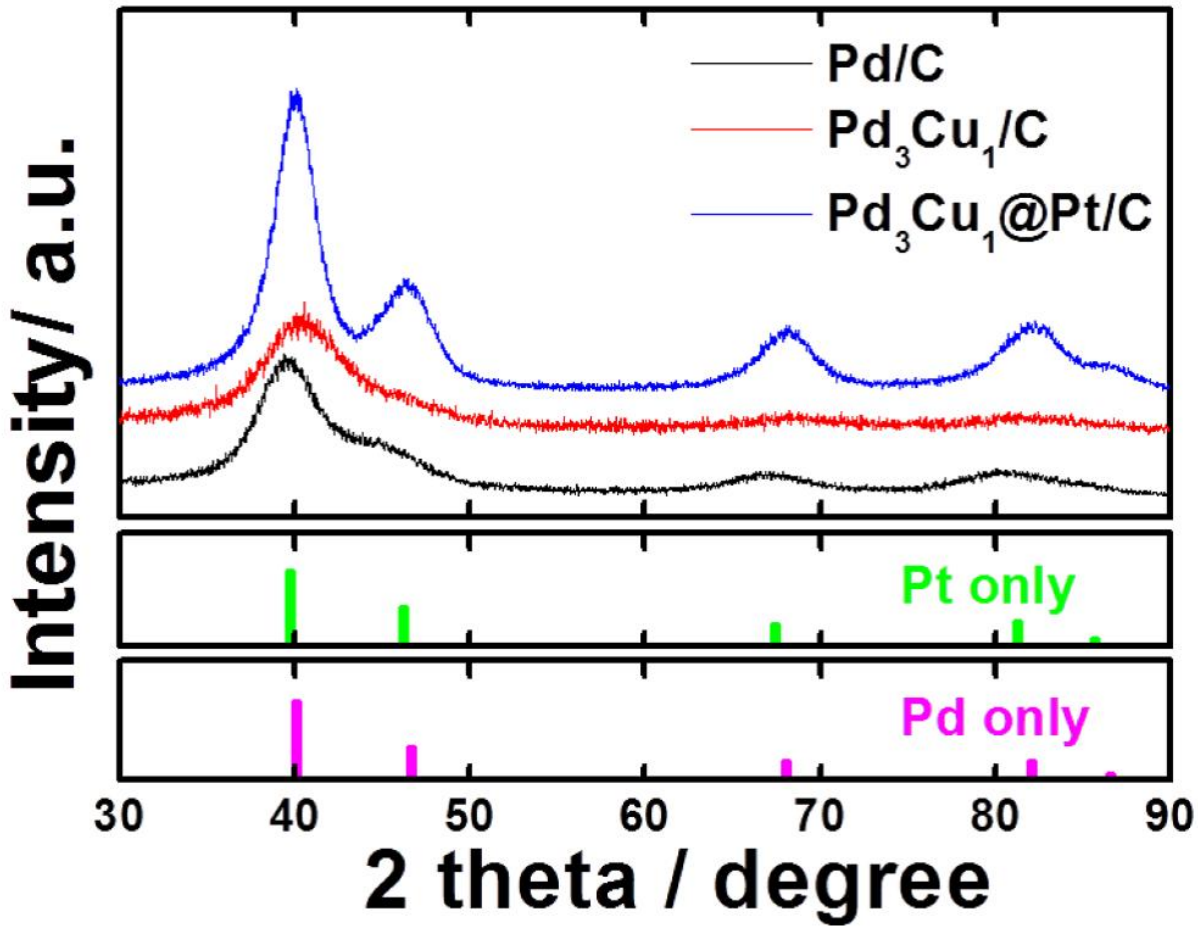

Fig. S12. X-ray diffraction patterns of the Pd/C, Pd_3Cu_1/C, and Pd_3Cu_1@Pt/C core-shell catalysts studied in this work.

2.2. X-ray Photoelectron Spectroscopy

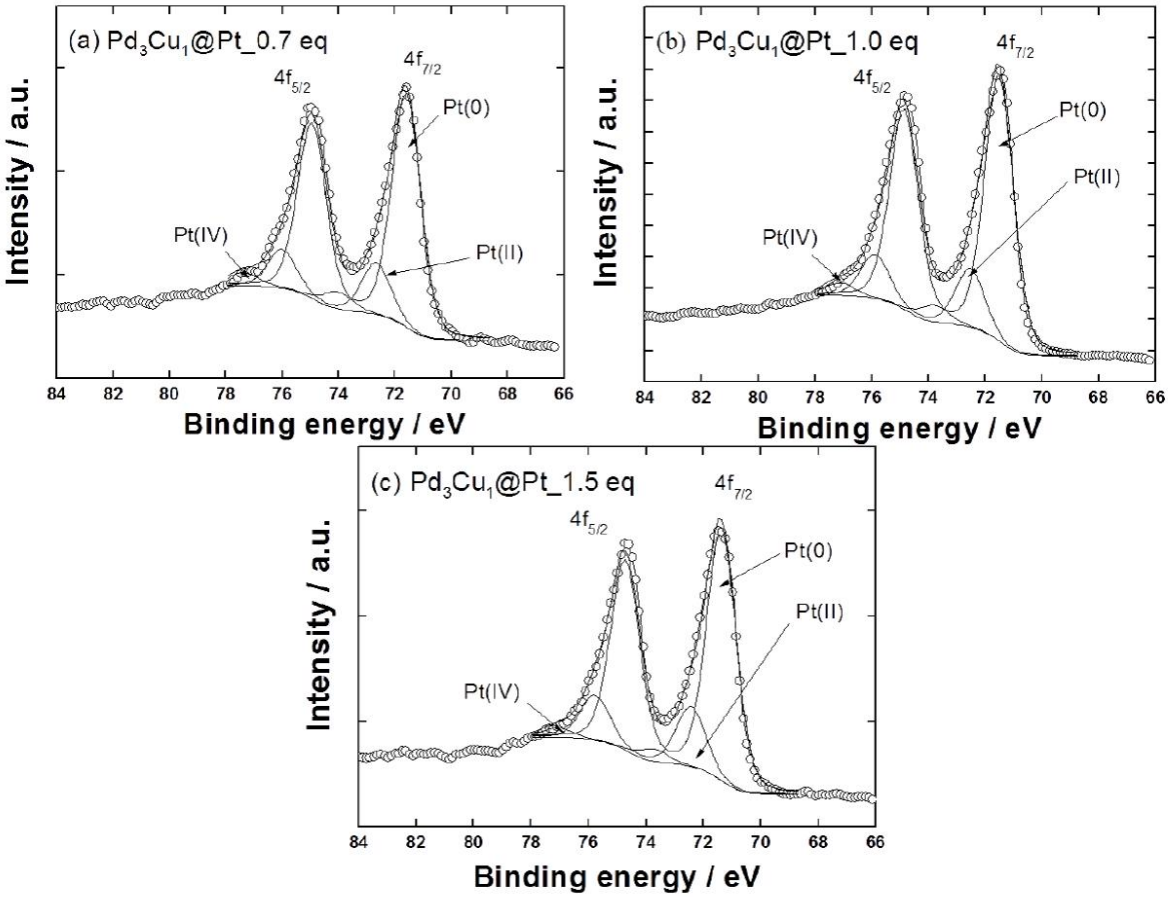

(d)

	Pt(0) / eV	Pt(II) / eV	Pt(IV) / eV	Pt(0): Pt(II): Pt(IV)
Pt 0.7 eq	71.60	72.66	74.01	77: 17: 6
Pt 1.0 eq	71.51	72.54	73.79	78: 17: 5
Pt 1.5 eq	71.37	72.43	73.73	78: 18: 4

Fig. S13. Pt 4f XPS fitting data of prepared core-shell electrocatalysts: (a) Pt: 0.7 eq, (b) Pt: 1.0 eq, (c) Pt: 1.5 eq, (d) Summary of binding energies and ratio of different Pt states.

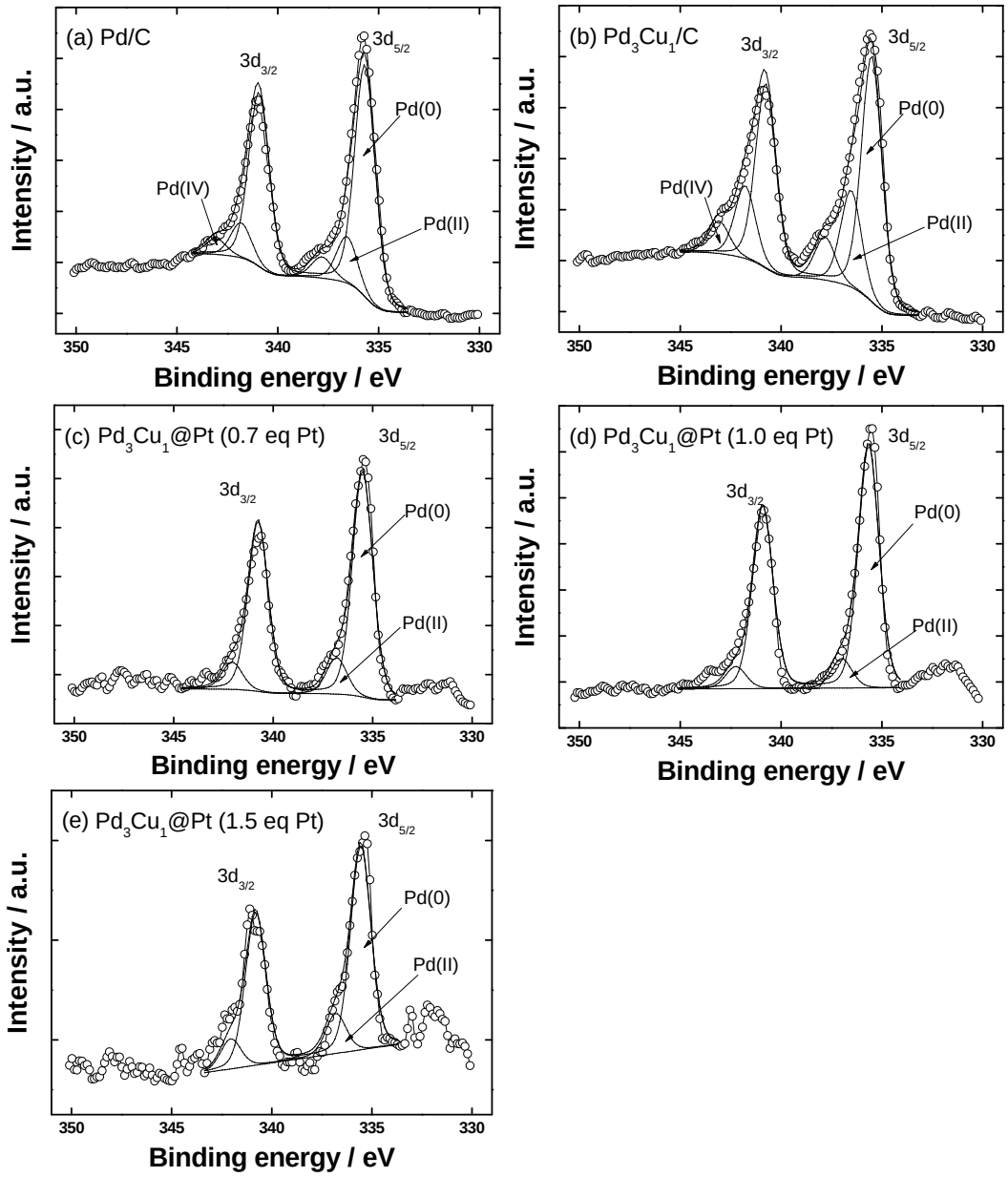

Fig. S14. Pd 3d XPS fitting data of prepared core-shell electrocatalysts: (a) Pd/C, (b) Pd_3Cu_1/C, (c) Pd_3Cu_1@Pt, Pt: 0.7 eq, (d) Pd_3Cu_1@Pt, Pt: 1.0 eq,(e) Pd_3Cu_1@Pt, Pt: 1.5 eq.

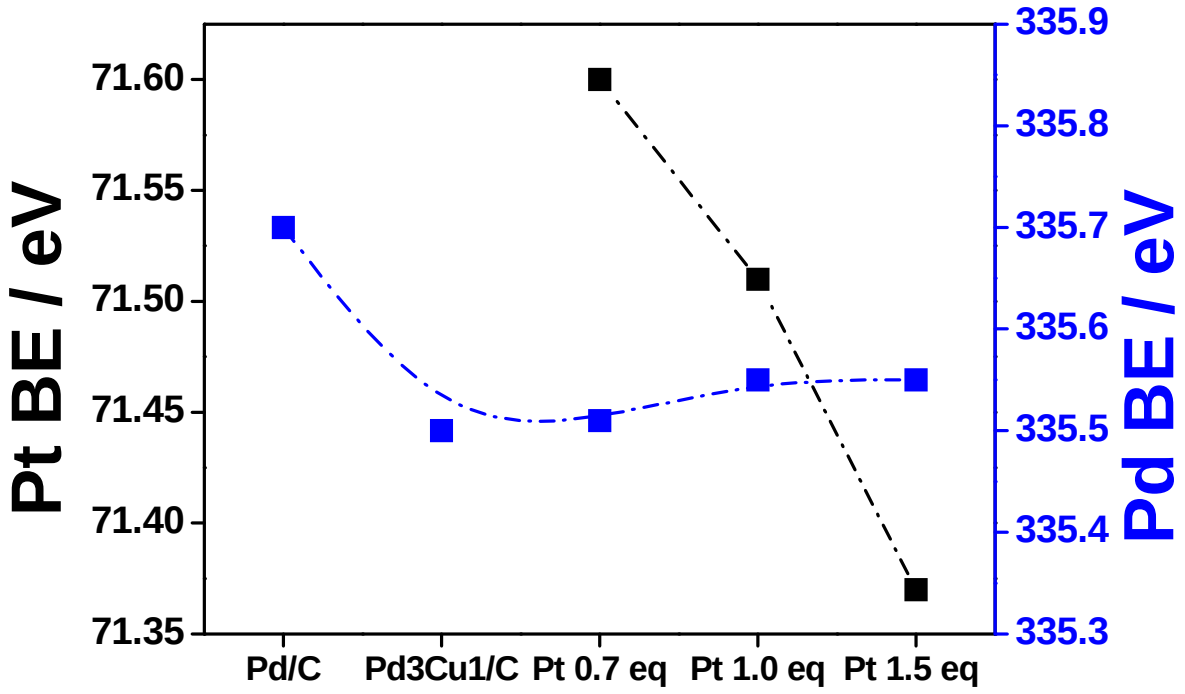

Fig. S15. Binding energy (BE) of Pt 4f and Pd 3d as a function of Pt layer thickness.

2.3. Synchrotron X-ray absorption spectroscopy

To evaluate this argument, we measured X-ray absorption near-edge spectroscopy (XANES) on carbon-supported Pd_3Cu_1@Pt with different shell thickness, and we measured the Pt L_{III} edges. One significant aspect of the XANES analysis is that it can provide important information on the Pt *d*-band vacancy. The *d*-band vacancy is derived from the analysis of the Pt L_{III} and L_{II} white lines. The L_{II} and L_{III} edges are due to the excitation of the $2p_{1/2}$ and $2p_{3/2}$ electrons, respectively. These electrons can undergo transitions to empty states in the vicinity of the Fermi level. Since the dipole selection rules in the XANES region restrict the transitions to L = 1 and J = 0, 1 (where L and J are the orbital angular quantum number and the total angular quantum number, respectively), the transitions to the *d*-orbitals are strongly favored[1]. In the case of Pt, it has been shown that the contribution of the final states with J = 5/2 is 14 times more than the contribution with J = 3/2. The L_{III} transition ($2p_{3/2}$ to $5d_{5/2}$) is thus more highly favored by the selection rules than the L_{II} transition ($2p_{3/2}$ to $5d_{5/2}$)[2]. The intensity of the L_{III} peaks, and to a lesser extent the L_{II} peaks, increases with increasing Pt *d*-band vacancy[3]. X-ray absorption near edge structure (XANES) experiments were conducted on 5A beamline of Pohang Accelerator Laboratory (PAL) (2.5 GeV; 150-180 mA). The incident beam was monochromatized using a Si(111) double crystal monochromator and detuned by 30% to minimize the contamination from higher harmonics, in particular, the third order reflection of the silicon crystals. The spectra for L_{III}-edge of Pt (E_0 =11564 eV) were taken in a transmission mode with separate He-filled IC Spec ionization chambers for incident and transmitted beams, respectively. Before measuring samples, energy was calibrated by using of Pt foil. The energy scan was performed in five regions for good energy resolution in a steep absorption and measurement of XANES spectra at a time, 5 eV-step in region of 11364-11514 eV, 1 eV-step in 11514-11554 eV, 0.25 eV-step in 11554-11594 eV, 0.03 *k*-step in 11594-12104 eV, and 0.04 *k*-step in 12104-12564 eV. Pre-edge absorption due to the background and detector were subtracted using a linear fit to the data in the range of -200 to -60 eV relative to E_0. E_0 was defined as the first inflection point on the rising absorption edge. Each spectrum was then normalized by a constant, extrapolated value to E_0 of third-order polynomial fit over absorption at 150-900 eV relative to E_0. The data analysis package used for XANES was the University of Washington's data analysis program. The XANES spectra were first subjected to background removal by fitting the pre-edge data to a Victoreen type formula over the range of -200 to 80 eV below the edge, followed by

extrapolation over the energy range of interest and subtraction from the data. After the removal of the background contributions, the spectra were corrected for edge-shifts using the second derivatives of the inflection points of the data from the reference channel. The procedures used for normalization were the conventional ones. The normalization value was chosen as the absorbance at the inflection point of one EXAFS oscillation.

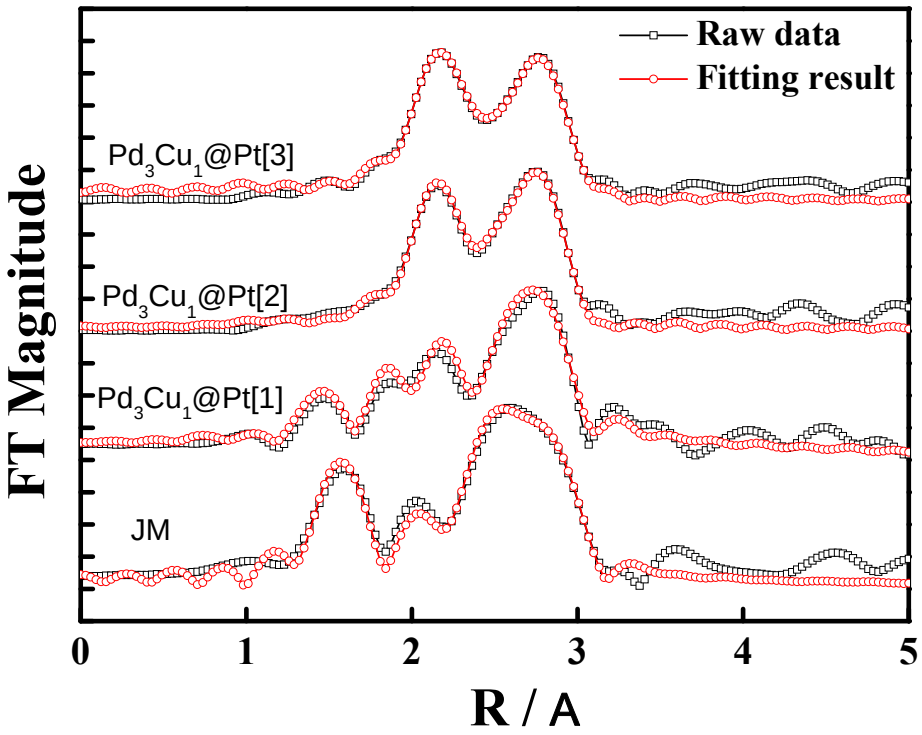

Fig. S16. Fourier transform (FT) magnitute of PtL_{III}-edge and interatomic distance with different shell thickness of Pd_3Cu_1@Pt.

Sample	Bond	N	R (Å)	σ^2 (Å^2)	ΔE (eV)	R_{factor} (%)
Pt/C (J.M.)	Pt-O	1.4	2.00	0.0033	6.1	0.6
	Pt-Pt	6.6	2.76	0.0066		
Pd_3Cu_1@Pt[1]	Pt-O	0.9	1.97	0.0033*	2.0	0.9
	Pt-Pt	3.0	2.68	0.0068		
	Pt-Pd	2.2	2.70	0.0068		
	Pt-Cu	0.9	2.63	0.0052		
Pd_3Cu_1@Pt [2]	Pt-O	1.0	2.00	0.0033*	2.9	0.1
	Pt-Pt	4.8	2.70	0.0075		
	Pt-Pd	1.8	2.72	0.0075		
	Pt-Cu	0.6	2.63	0.0052		
Pd_3Cu_1@Pt [3]	Pt-O	0.8	2.04	0.0033*	4.3	0.1
	Pt-Pt	6.0	2.73	0.0079		
	Pt-Pd	1.7	2.74	0.0079		
	Pt-Cu	0.5	2.64	0.0052		

1. Notation: *N*, coordination number; *R*, interatomic distance; σ^2, Debye-Waller factor; *ΔE*, energy-shift; *R-factor*, goodness of fit which gives a sum-of-squares measure of the fractional misfit.
2. *fixed parameter.
3. The value in parenthesis denotes the estimated error of the calculated parameter.

Table S1. Results of model fitting of k^3-weighted and Fourier-filtered Pt L_{III} EXAFS for Pd_3Cu_1@Pt.

3. Electrochemical analysis using a rotating disk electrode

Electrochemical measurements: The catalyst ink was prepared by mixing 10 mg of carbon supported nanoparticles with 50 µL of DI water, 100 µL of nafion as a binder material, and 1mL of isopropyl alcohol. Follow mixing and ultrasonification, 7µL of ink slurry was pipetted onto a glassy carbon substrate. The dried electrode was then transferred to the electrochemical cell for electrochemical measurements. Cyclic voltammetry (CV) and linear sweep volatammetry (LSV) were performed using an Autolab PGSTAT20 potentiostat and a rotating disk electrode (RDE) system (Pine) in a standard three-electrode configuration. An deposited glassy carbon electrode with a diameter of 5 mm was used as the working electrode and a platinum wire was used as the counter electrode. All the electrochemical measurements, except for the ORR and HOR with the RDE configuration, were performed in an Ar-purged 0.1 M $HClO_4$ solution. For the ORR and HOR experiment, 99.99 % oxygen and hydrogen gas were bubbled into the electrolyte for 30 min before each measurement respectively. Before each measurement, the glassy carbon electrode was polished with a 0.05-µm alumina paste followed by washing with distilled (DI) water in an ultrasonic bath. A saturated calomel electrode (SCE) with 3 M KCl (Gamry) and Pt mesh were used as the reference and counter electrodes, respectively. However, in this paper, all the potentials reported are with respect to the Reversible Hydrogen Electrode (RHE).

The ORR measurements were performed in 0.1 M $HClO_4$ solutions under flow of O_2 (research grade) using the glassy carbon rotating disk electrode (RDE) at a rotation rate of 1600 rpm and a sweep rate of 10 mV s^{-1}. In order to produce a clean electrode surface, several potential sweeps between 0.05 and 1.1 V versus RHE were applied to the electrode prior to the ORR measurement. In the ORR polarization curve, current densities were normalized in reference to the geometric area of the glassy carbon RDE (0.196 cm^2).

For the ORR at a RDE, the Koutecky-Levich equation can be described as follows:

$$1 / i = 1 / i_k + 1 / i_{l,c} = 1 / i_k + 1 / (0.62nFAD_0^{2/3}\omega^{1/2}\nu^{-1/6}C_0^*) \quad (1)$$

where i is the experimentally measured current, $i_{l,c}$ is the diffusion-limiting current, and i_k is the kinetic current; where D_0 is the diffusivity of oxygen in 0.1 M $HClO_4$ (estimated from the product of O_2 diffusivity at infinite dilution and the ratio of the dynamic viscosities of the

electrolyte and pure water), n is the number of electrons in the O_2 reduction reaction (*i.e.*, $n = 4$), ν is the kinematic viscosity of the electrolyte, c_0 is the solubility of O_2 in 0. 1 M $HClO_4$, and ω is the rotation rate. Then, the kinetic current was calculated based on the following equation:

$$i_k = (i \times i_{l,c}) / (i_{l,c} - i) \quad \text{---------- (2)}$$

The HOR on the Pt-based electrocatalysts in the aqueous electrolyte is faster than other electrochemical reactions. Therefore, the concentrations of H_2 gas dissolved in the aqueous electrolyte are exhausted near the electrode, which means that the reaction is no longer kinetically controlled. For this reason, the rotating disk electrode (RDE) technique has conventionally been used to investigate the kinetics of reactions such as the electrocatalysis of the HOR in order to maintain steady-state conditions. We studied the kinetics of the HOR on PdIr alloy and Pd@PdIr core-shell electrodes and compared the kinetics of PdIr alloys, Pd@PdIr core-shell, and pure Pt. The polarization curves for the RDEs in sulfuric acid saturated with H_2 gas at 276 K, obtained using a sweep rate of 20 mV/s in the range from 0.0 to 0.3 V at different rotational speeds from 1000 to 3000 rpm are displayed in fig. S18. The current density, with respect to the activation and diffusion, is described by the following equation:

$$1/i = 1/i_k + 1/i_d \quad \text{------ (1)}$$

Here, ik is the kinetic current and id is the current of diffusion in the electrolyte. The diffusion current, i.e. the current that is determined by the rate of supply of dissolved hydrogen to the surface, was calculated with the Levich equation:

$$i_d = 0.62nFD^{2/3}v^{-1/6}\, C_0\omega^{0.5} \quad \text{------ (2)}$$

Here, n is the number of electrons, F is Faraday's constant, D is the diffusion coefficient for hydrogen in the electrolyte, v is the kinematic viscosity of the electrolyte, c_0 is the hydrogen concentration in the electrolyte, and ω is the electrode rotation rate. C_0, v, and D were calculated based on Henry's law, the method reported in reference, and the Stokes-Einstein equation, respectively. Then, given (2), formula (1) assumes the form of the following equation:

$$1/i = 1/i_k + 1/(Bc_0\omega^{0.5}) \quad (3)$$

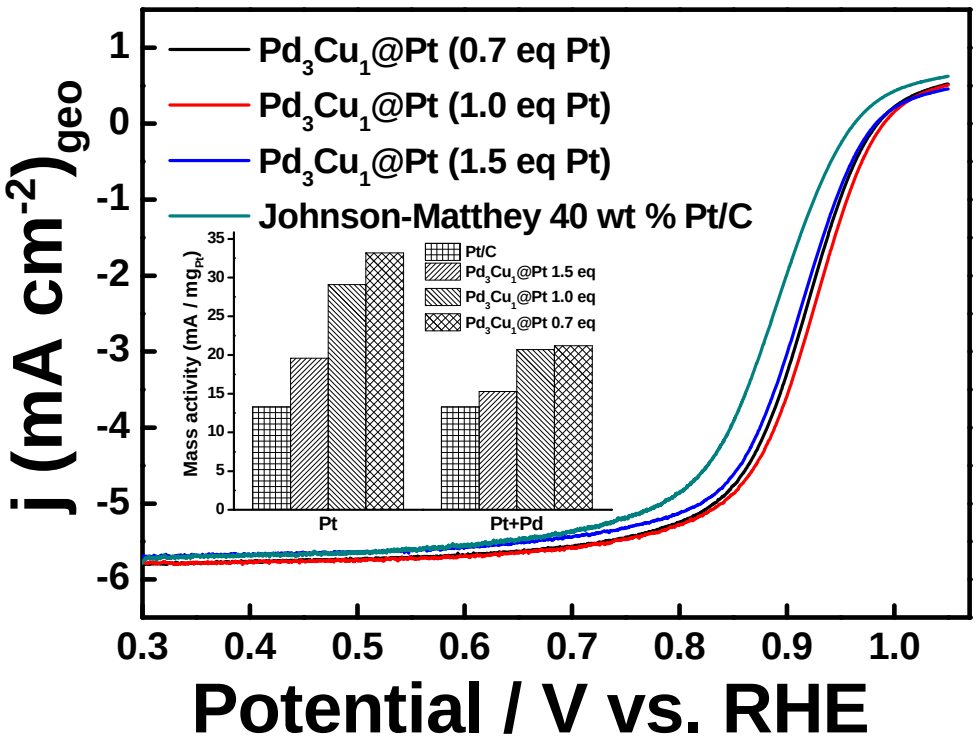

Fig. S17. ORR polarization curves for Pd_3Cu_1@Pt core@shell electrocatalysts with variation of shell thickness. Mass-specific activity is given as a kinetic current density ik that is normalized in reference to the loading amount of Pt and Pt and Pd.

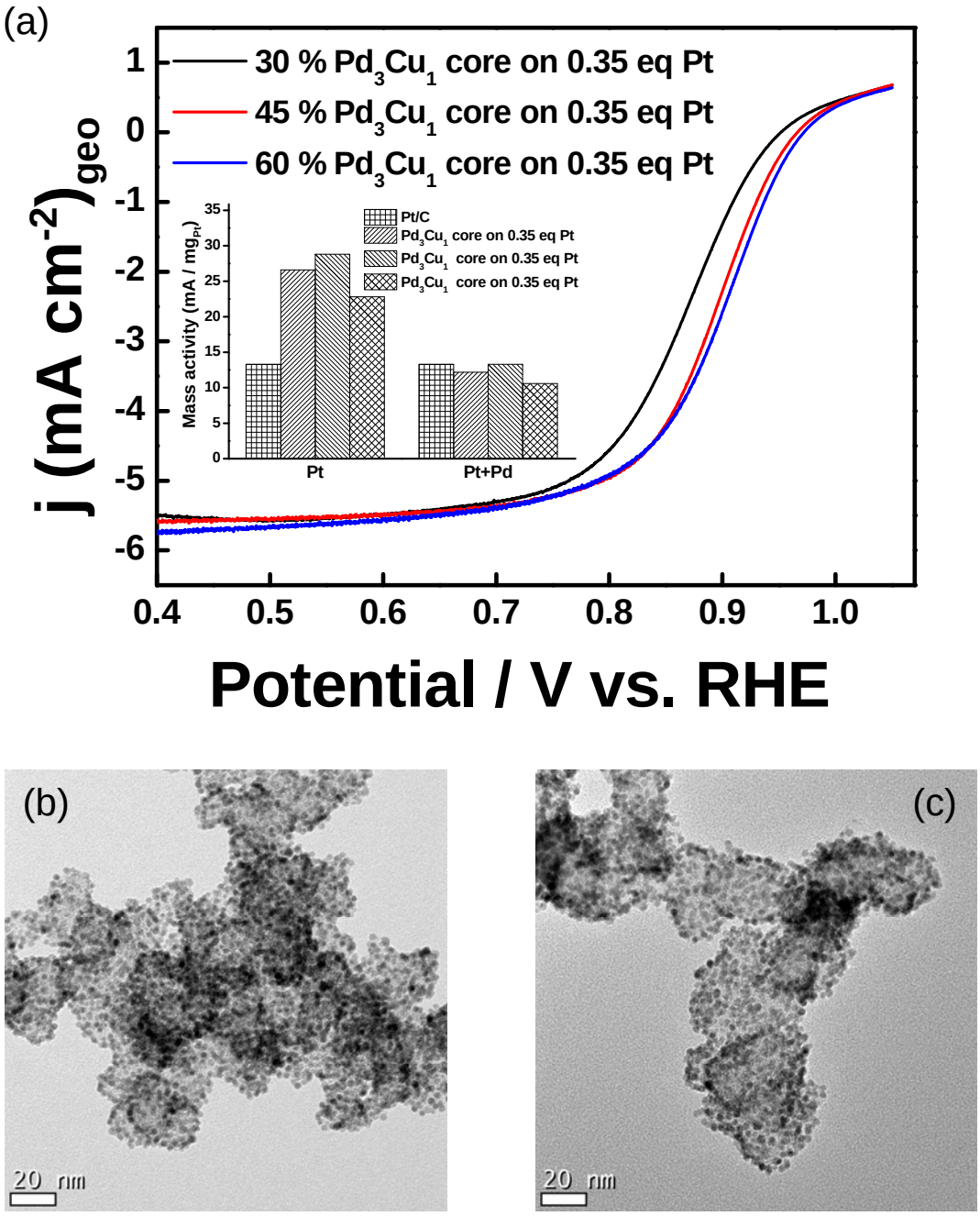

Fig. S18. (a) ORR polarization curves for 0.35 eq Pt coated core@shell electrocatalysts with variation of core size. Mass-specific activity is given as a kinetic current density ik that is normalized in reference to the loading amount of Pt and Pt and Pd. The numbers of 30, 45, and 60 imply the loading amounts of cores with respect to the mass of carbon supports. TEM images of cores with different loading amounts are also shown; (b) 30% and (c) 45%.

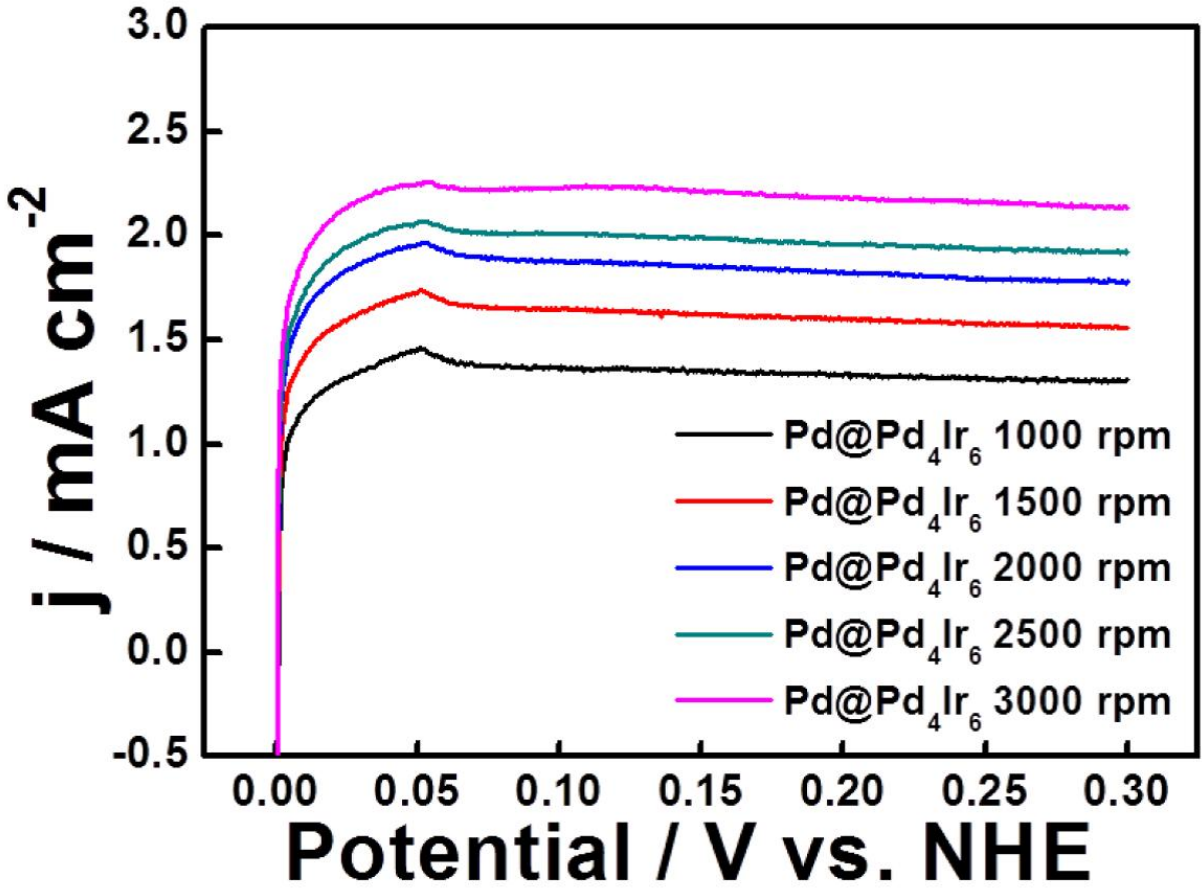

Fig. S19. Hydrogen oxidation current densities during positive-going sweeps (20 mV/s) on $Pd@Pd_4Ir_6$ core-shell catalysts in 0.5 M H_2SO_4 saturated with H_2 at 273 K.

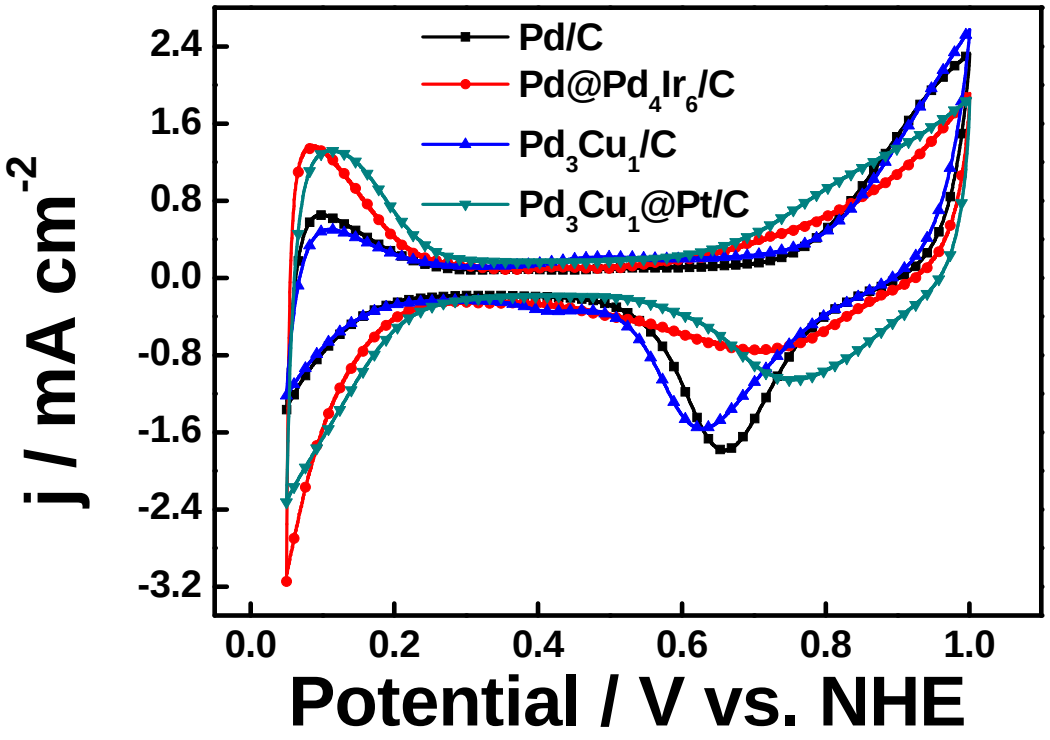

Fig. S20. Cyclic voltammograms of prepared core NPs (Pd/C and Pd_3Cu_1/C) and core@shell NPs (Pd_3Cu_1@Pt/C and Pd@PdIr/C) in Ar-saturated 0.1 M $HClO_4$ solution at 298 K with the sweep rate of 20 mV/s.

4. Single Cell Operation

Single cell fabrication and evaluation: 40 wt % Johnson-Matthey Pt/C and prepared core@shell electrocatalysts were used as cathode catalysts for the preparation of Pt/C MEA and Pd_3Cu_1@Pt MEA, respectively. Catalyst ink was prepared ultrasonically using carbon-supported Pt and core-shell powder and ionomers (5 wt % Nafion solution, Aldrich) in a mixture of isopropyl alcohol in deionized water as a solvent. Then, prepared catalyst ink was directly coated onto the fixed membrane by spraying method. The active area of the MEA was 10 cm^2 and 0.2 mg/cm^2 of Pt (with JM Pt/C) was loaded onto the anode and 0.3 mg/cm^2 of metal onto cathode (In the case of Pd_3Cu_1@Pt core@shell catalyst, 0.218 $mgPt/cm^2$ was used). The MEA was comprised of a single cell (CNL-PEM005-01, CNL Energy) with gas diffusion microporous layers, and the single-cell was connected to a fuel cell test station (CNL Energy) in order to evaluate performance and degradation in a simulated mode. Humidified hydrogen and air were fed to the anode and cathode sides of the single cell at a temperature of 75/70 ◦C. Then, the temperature and pressure of the single cell were maintained at 70 ◦C and ambient pressure during the operation. To investigate the fuel cell performance, polarization curves were obtained using a fuel cell test station for each MEA. The degradation tests were carried by load cycling and constant current mode for evaluating durability of MEA with core-shell electrocatalysts. The load cycling procedure involved two steps: in step 1, the load was increased 50 mAs^{-1} from OCV to 0.35 V, whereas in step 2, the load was shut off at 0.35 V and kept OCV for 30 s. The load cycling procedure was repeated for 3,000 min.

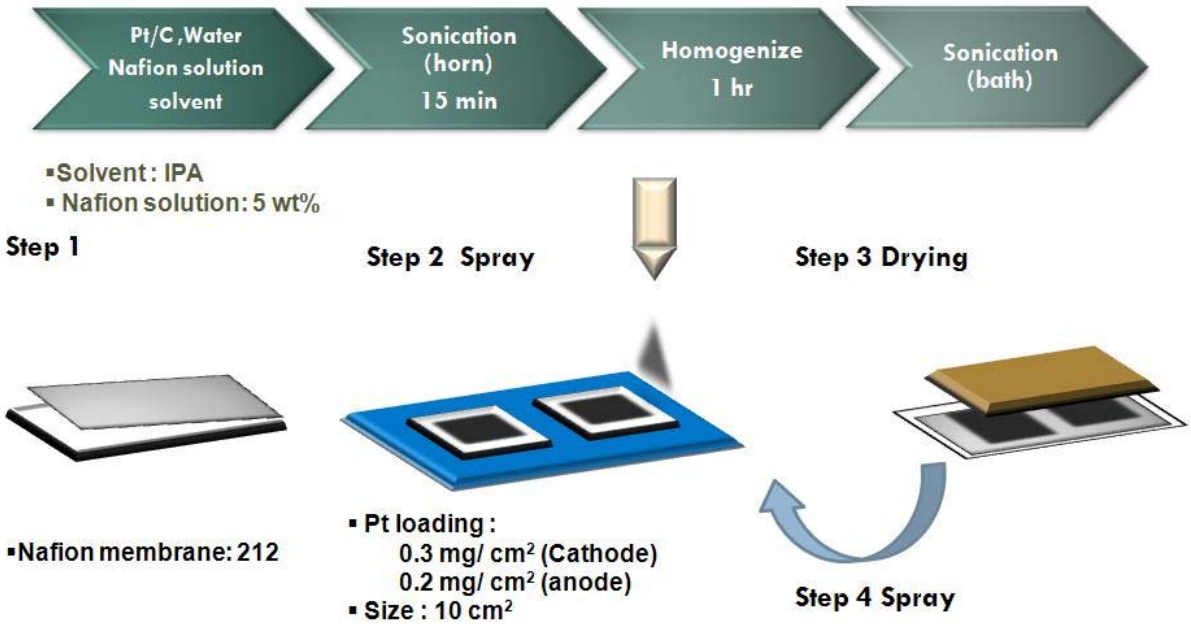

Fig. S21. Brief description of preparation process of MEA by catalyst-coated membrane (CCM) spray method.

5. Computation method using DFT calculation

5.1 Computational Detail:

- VASP: the first principle calculation program by using a planewave basis set and pseudopotential method.
- Projector augmented wave (PAW) potential
- Exchange-correlation (XC) functional: Generalized gradient approximation (GGA) by Perdew-Burke-Ernzerhof (PBE)
- Cut off energy : 400 eV
- Non-spin polarized calculation: Pt/Pd (-0.009 eV), Pt/Ir (same), Pt (same) and Pt/Pd_3Cu_1 (-0.001 eV)
  - For these materials systems, spin polarized and non-spin polarized calculations gave the same energies or very small differences as the value in parenthesis.
- Spin collinear calculation: Pt/Ni (-1.66 eV), Pt/Pd_3Fe_1 (-10.57eV), Pt/Pd_3Co_1 (-4.28eV), Pt/Pd_3Ni_1 (-0.84eV), and Pt_3Ni_1 (-0.25eV)
  - Lower energy as the value in parenthesis than that of non-spin polarized calculation
- Brillouin zone sampling: 7x7x1 k-points grids based on gamma-centered point.

5.2 Model:

- Calculation of adsorption energies (E_{ad}) and vacancy formation energies (E_{vac}) for Pt skin on various sublayers
  - Pure metal sublayer: Pt/Ni, Pt/Pd, Pt/Ir and Pt
  - Binary metal sublayer based on Pd: Pt/Pd_3Fe_1, Pt/Pd_3Co_1, Pt/Pd_3Ni_1 and Pt/Pd_3Cu_1
  - Binary metal sublayer based on Pt: Pt/Pt_3Ni_1
- Crystal structure: face-center cubic (FCC) structure
- Lattice constants for slab models: values obtained by bulk calculation for each elements
  - Numbers in parenthesis are experimental values and the differences (%) with reference to the experiments.
  - Bulk Ni: 3.52 Å (3.52 Å, 0.0 %)

- Bulk Pd: 3.95 Å (3.89 Å, +1.5 %)
- Bulk Ir: 3.88 Å (3.84 Å, +1.0 %)
- Bulk Pt/Pd_3Fe_1: 3.90 Å
- Bulk Pt/Pd_3Co_1: 3.87 Å
- Bulk Pt/Pd_3Ni_1: 3.87 Å
- Bulk Pd_3Cu_1: 3.98 Å
- Bulk Pt/Pt_3Ni_1: 3.89 Å

- Surface design: Pt(111) slab model with *p*(2x2) supercells

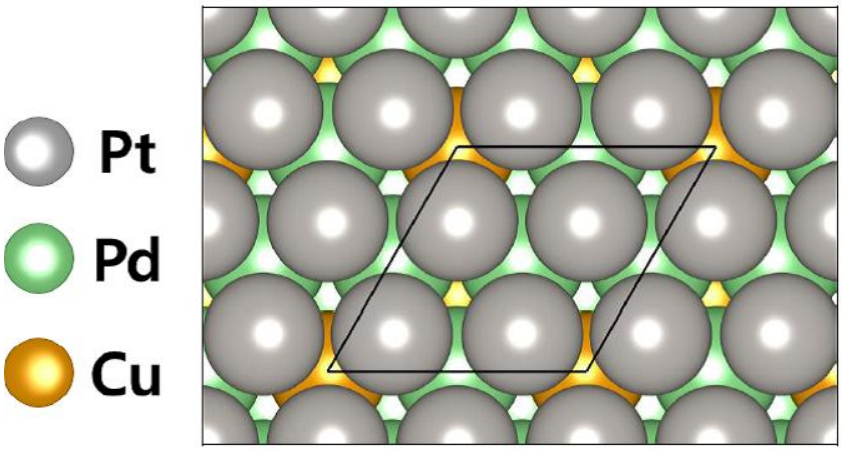

Fig. S22. The Pt(111)-p(2x2) surface on Pd_3Cu_1. The Pd, Cu and Pt atoms are colored green, orange and gray, respectively.

- Stability test between B (fcc stacking sequence) and C layer (hcp stacking sequence) as Pt shell on various sublayers.
  - For all systems, B layer is more stable than C layer.

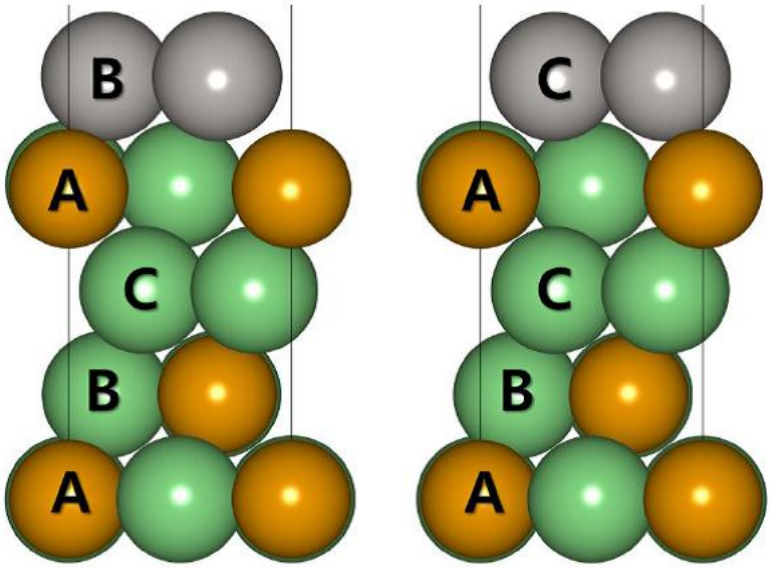

Fig. S23. Packing sequence of A, B and C layer. The Pd, Cu and Pt atoms are colored green, orange and gray, respectively.

- Slab models: total eight atomic layers and the bottom two layers were fixed during relaxation.
  - Pt shell thickness: thickness of Pt layers has been changed from one to four atomic layers while total number of layers was fixed to eight.
  - Vacuum thickness: 20 Å

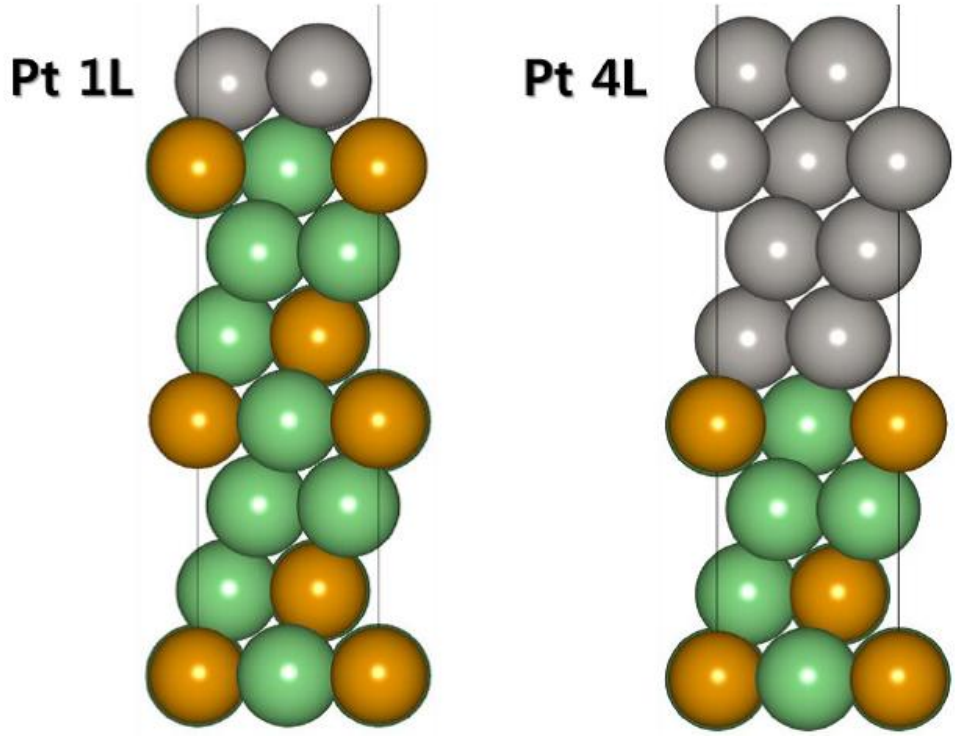

Fig. S24. Side view of 2x2x8 supercell. The Pd, Cu and Pt atoms are colored green, orange and gray, respectively.

- Vacancy formation energy (E_{vac})
  - This energy can be used as a measure of stability of Pt surface. This is related to the bond strength of Pt atoms in Pt surface.
    - Surface stability: calculation of energy difference as a Pt atom separate from the surface
    - Single point calculation with increasing distance between the separated Pt atom and the surface
    - Maximal energy difference = vacancy formation energy (E_{vac})
  - $E_{vac} = E_{total}^{N,clean} - \left(E_{total}^{N-1} + E_{total}^{Atom}\right)$
    - N: the number of total atoms in the slab model
  - Symmetrically two distinct sites of Pt on Pd_3Cu_1
    - "Up site" Pt: Pt on 3 Pd atoms: slightly higher position than Cu atom of same layer
    - "Down site" Pt: Pt on 2 Pd, 1 Cu atom: slightly lower position than Pd atom of same layer
    - The vacancy formation energy of Pt on Pd_3Cu_1 was averaged for all the surface atoms.

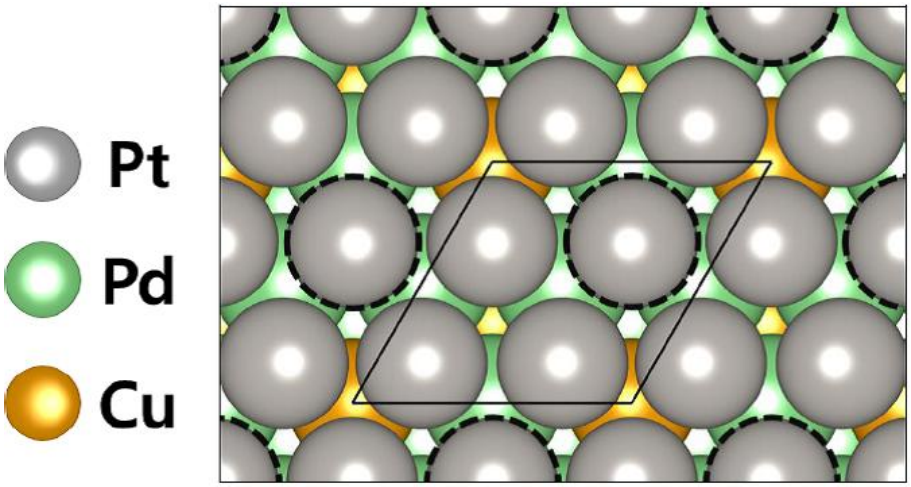

Fig. S25. Two symmetrically different sites of Pt on Pd_3Cu_1. The Pd, Cu and Pt atoms are colored green, orange and gray, respectively. The atoms which be surrounded by broken black line corresponds to "Up site" atoms.

- Adsorption energy (E_{ad})
  - $E^{ad} = E_{total}(O - Pt/Pd_2Cu) - E_{total}(Pt/Pd_3Cu) - 1/2E_{total}(O_2)$
  - Eight symmetrically distinct adsorption sites of O on Pt/ Pd_3Cu_1

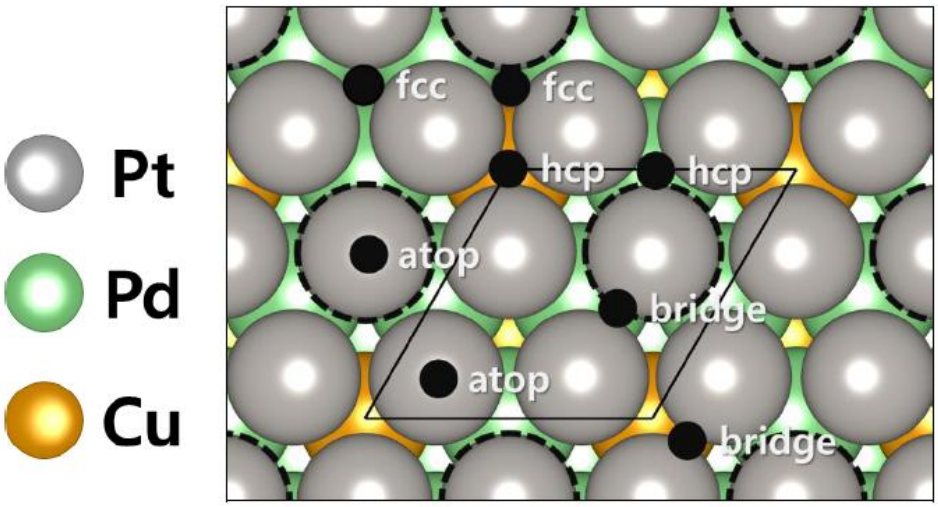

Fig. S26. Possible adsorption sites of O on Pt/ Pd_3Cu_1 surface. The Pd, Cu and Pt atoms are colored green, orange and gray, respectively. The atoms which be surrounded by broken line is "Up site" atoms.

Results:

- Vacancy formation energy and oxygen adsorption energy with various thickness of Pt overlayer
  - Pt thickness effect: E_{vac} and E_{ad} of thicker Pt overlayer than 1 monolayer approached to that of pure Pt
  - Pd_3Cu_1@Pt with Pt 1 monolayer
    - Increase as 0.34 eV than that of pure Pt in E_{vac}: better stability
    - Decrease as 0.24 eV than that of pure Pt in E_{ad}: better reactivity

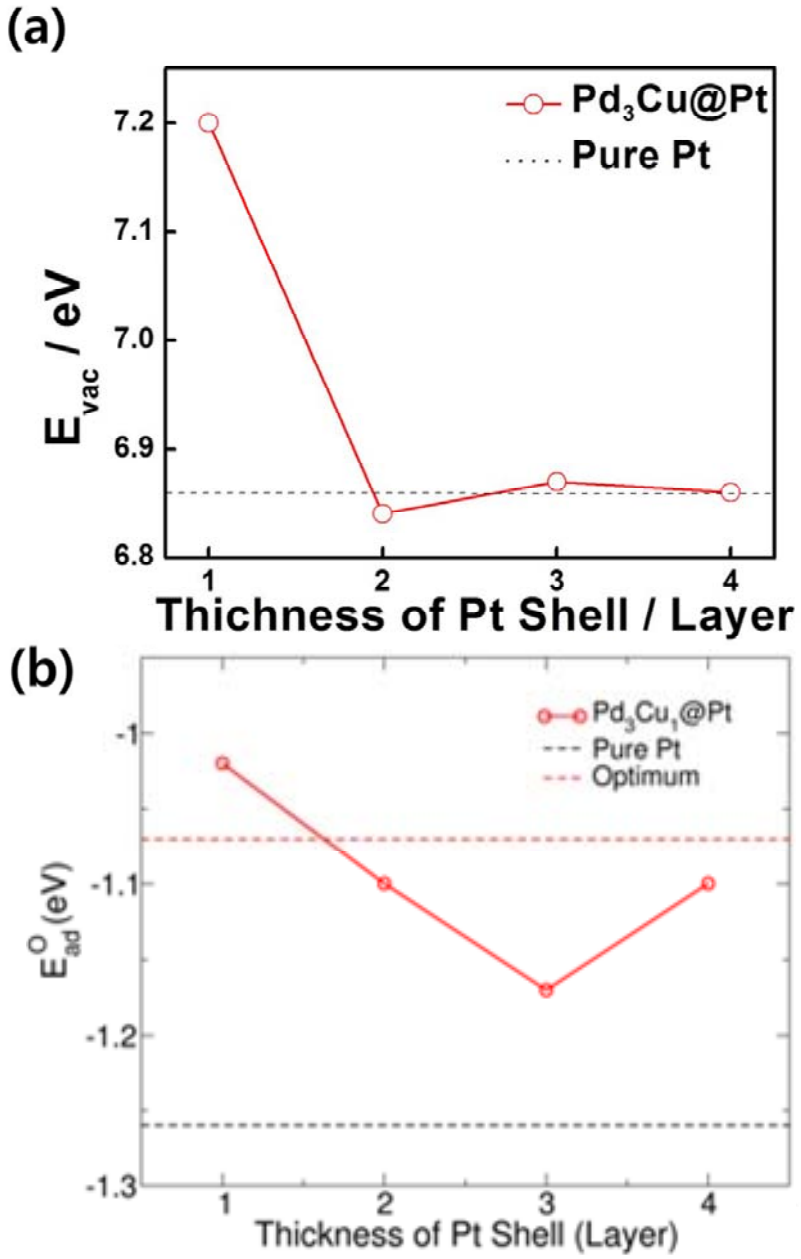

Fig. S27. (a) Vacancy formation energy and (b) oxygen adsorption energy with various thickness of Pt over-layer.

5.3 Bader charge analysis:

- The estimated Bader charge for all the elements
- From 3 to 6 atomic layers: bulk property in the subsurface
- Charge transfer were found for the Pt and PdM(M=Fe, Co, Ni, Cu) systems.

	Pt	Pd, Fe	Pd, Co	Pd, Ni	Pd, Cu
Bulk (5L)	10.00	10.23, 7.29	10.15, 8.53	10.10, 9.69	10.10, 10.70
Bulk (6L)	9.99	10.22, 7.29	10.14, 8.53	10.10, 9.69	10.09, 10.70
Interface (7L)	9.96	10.09, 7.20	10.04, 8.43	10.00, 9.60	9.99, 10.64
Surface Pt (8L)	10.05	10.15	10.13	10.11	10.11

Table S2. Estimated Bader charge of the subsurface and surface. The Bader charge was averaged for each layer.

5.4 Local density of states (LDOS)

- Local density of states (LDOS) plot at Fermi level
  - Local PDOS for d-band of the pure Pt and various Pd alloys at Fermi level
  - LDOS: Pt > Pd_3Cu_1@Pt > Pd_3Ni_1@Pt > Pd_3Co_1@Pt > Pd_3Fe_1@Pt
  - LDOS at Fermi level is related to oxygen adsorption energy

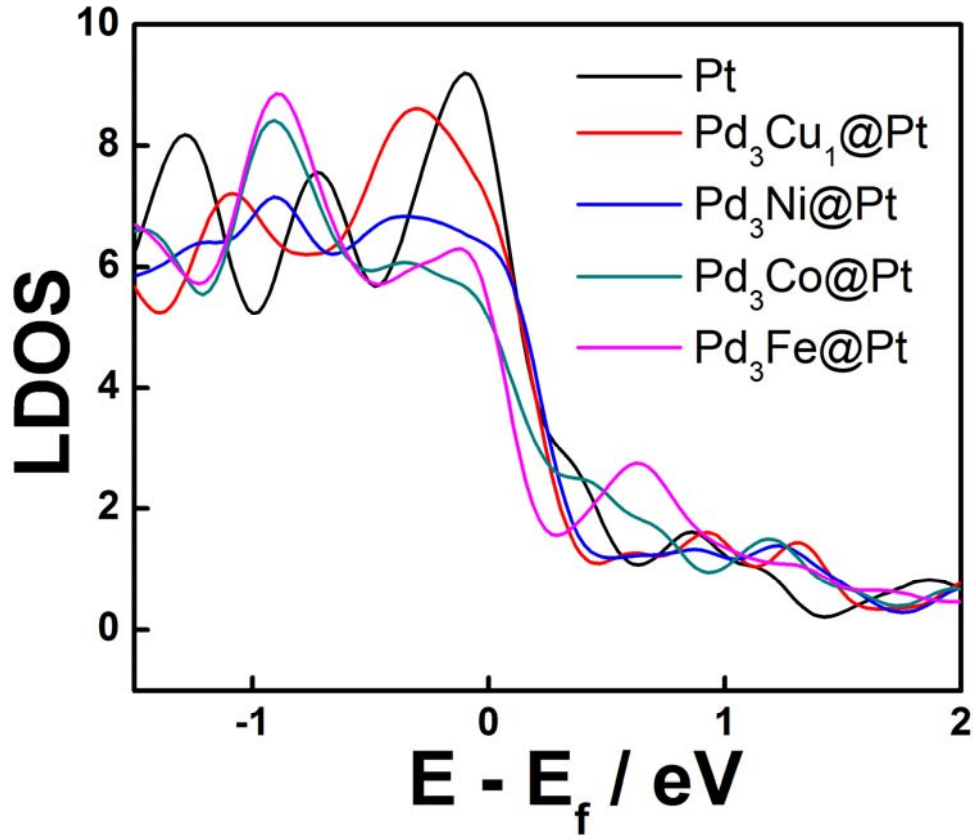

Fig. S28. LDOS at Fermi level for the pure Pt and various Pd alloys as core materials.

5.5 Charge density difference

- Charge density difference (ρ_{diff})
  - $\rho_{diff} = \rho_{total} - \left(\rho_{sublayer} + \rho_{overlayer}\right)$
  - Charge transfer: charge accumulation along the Pt and PdM interface (M=Fe, Co, Ni, Cu) layer
  - Hexagonal ring: three Pd and three Pt atoms belong to the ring for the Pd_3Cu_1 system (Figure (b))
  - Triangular shape: PdFe, PdCo and PdNi (Figure (c), (d), (e))

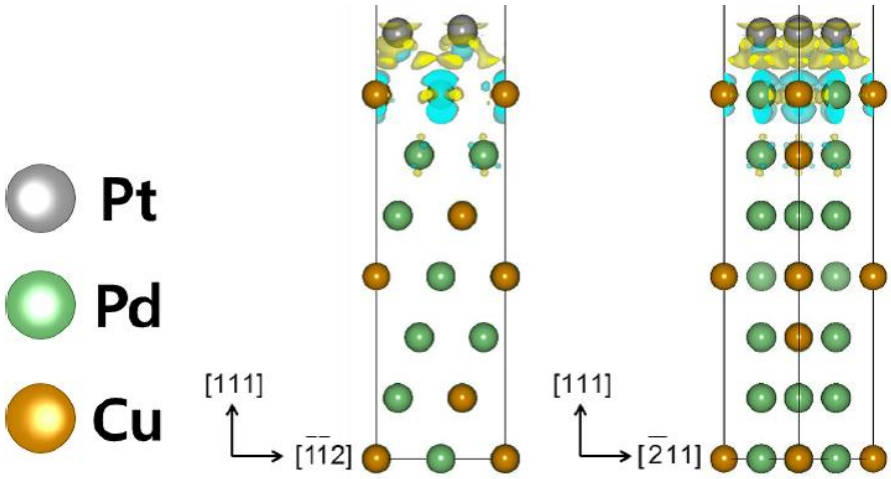

(a) Side view for Pd_3Cu_1@Pt

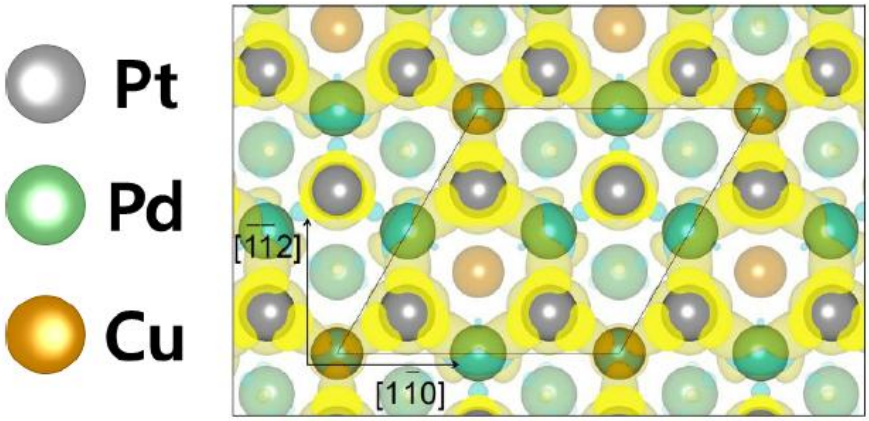

(b) Top view for Pd_3Cu_1@Pt. The Cu atoms are colored orange.

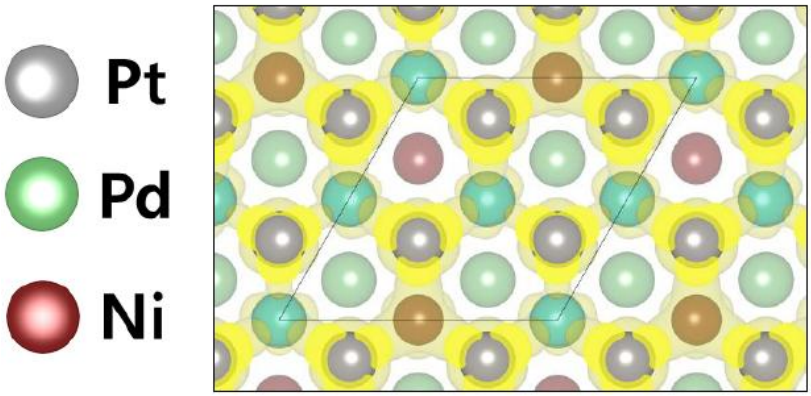

(c) Top view for Pd_3Ni_1@Pt. The Ni atoms are colored wine.

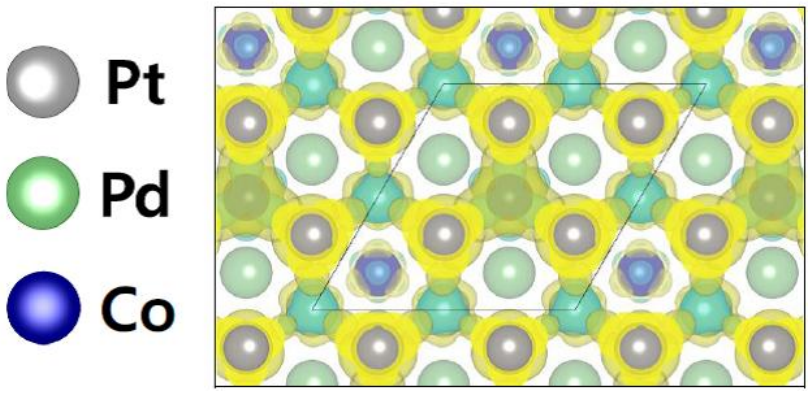

(d) Top view for Pd_3Co_1@Pt. The Co atoms are colored deep blue.

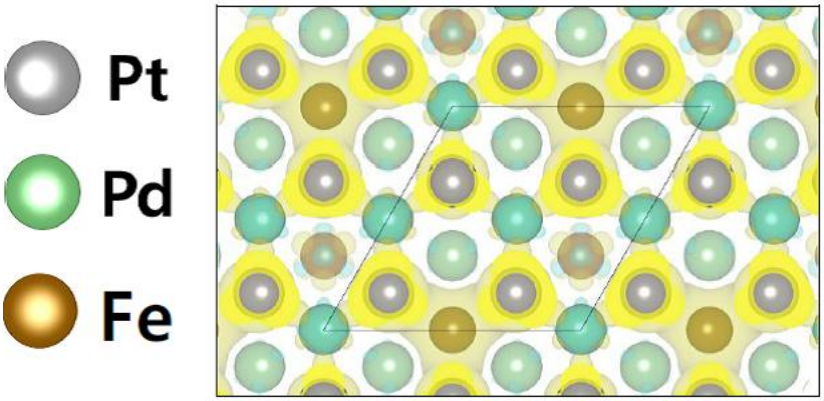

(e) Top view for Pd_3Fe_1@Pt. The Fe atoms are colored ocher.

Fig. S29. Charge density difference. The Pd and Pt atoms are colored green and gray, respectively. Increase and decrease of charge density are colored yellow and sky-blue. Intersection is colored blue color.

References

1. L. M. Falicov, W. Hanke, M. P. Maple, *Valence Fluctuation in Solids*, Nprth-Holland Pub., Amsterdam, **1981**.
2. A. E. Russell, S. Maniguet, R. J. Mathew, J. Yao, M. A. Roberts, D. Thompsett, *J. Power Sources* **2001**, *96*, 226.
3. A. N. Mansour, J. W. Cook, D. E. Sayers, *J. Phys. Chem.* **1984**, *88*, 2330.